

# Airfoil trailing-edge noise and drag reduction at a moderate Reynolds number using wavy geometries <sup>EP</sup>

Cite as: Phys. Fluids **34**, 117107 (2022); <https://doi.org/10.1063/5.0120124>

Submitted: 11 August 2022 • Accepted: 30 September 2022 • Published Online: 02 November 2022

Published open access through an agreement with JISC Collections

 T. A. Smith and  C. A. Klettner

## COLLECTIONS

 This paper was selected as an Editor's Pick



View Online



Export Citation



CrossMark

## ARTICLES YOU MAY BE INTERESTED IN

[Effects of phase difference on hydrodynamic interactions and wake patterns in high-density fish schools](#)

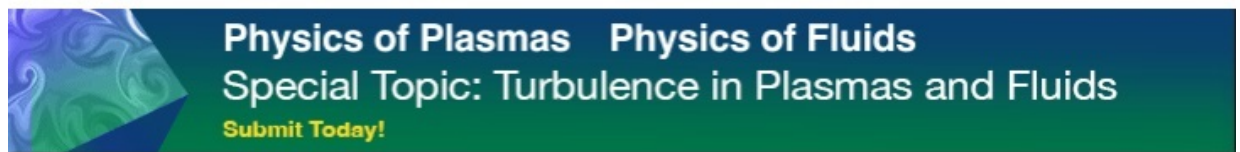
Phys. Fluids **34**, 111902 (2022); <https://doi.org/10.1063/5.0113826>

[Estimating forces from cross-sectional data in the wake of flows past a plate using theoretical and data-driven models](#)

Phys. Fluids **34**, 111905 (2022); <https://doi.org/10.1063/5.0125374>

[Numerical investigation of a propeller operating under different inflow conditions](#)

Phys. Fluids **34**, 105118 (2022); <https://doi.org/10.1063/5.0109801>



Physics of Plasmas   Physics of Fluids  
Special Topic: Turbulence in Plasmas and Fluids  
Submit Today!

# Airfoil trailing-edge noise and drag reduction at a moderate Reynolds number using wavy geometries

Cite as: Phys. Fluids **34**, 117107 (2022); doi: [10.1063/5.0120124](https://doi.org/10.1063/5.0120124)  
Submitted: 11 August 2022 · Accepted: 30 September 2022 ·  
Published Online: 2 November 2022



View Online



Export Citation



CrossMark

T. A. Smith<sup>a)</sup>  and C. A. Klettner 

## AFFILIATIONS

Department of Mechanical Engineering, University College London, London WC1E 7JE, United Kingdom

<sup>a)</sup> Author to whom correspondence should be addressed: [tom.smith.17@ucl.ac.uk](mailto:tom.smith.17@ucl.ac.uk)

## ABSTRACT

This study utilizes a hybrid aeroacoustic model to investigate how airfoils with spanwise wavy geometries can be used to reduce trailing-edge noise alongside improving the aerodynamic performance. A smooth airfoil is compared to four variants, which have spanwise surface waves of different wavelengths, at a Reynolds number of  $Re = 64\,000$  and an angle-of-attack of  $1^\circ$ . The first three variants have a geometry modified by a single wavelength, whereas the fourth has a surface composed of two wavelengths, which creates a more irregular surface variation. The results show that modest noise reductions of around 4 dB are achieved for the first three variants, but a much larger reduction of 17.7 dB is achieved for the fourth variant. The mechanisms behind the noise reduction are explored, and it is shown that the geometry reduces the spanwise correlation of the pressure fluctuations and also modifies the boundary layer dynamics, which contributes to the large reduction. It is further shown that a wavy geometry can reduce the drag force by reducing the shear stress over parts of the airfoil surface and by limiting the flow separation on the suction side. The fourth variant is also assessed across a wider range of angles ( $0^\circ \leq \alpha \leq 4^\circ$ ) and is shown to produce less noise than the smooth wing across the entire range as well as a drag reduction for  $\alpha \geq 1^\circ$ .

© 2022 Author(s). All article content, except where otherwise noted, is licensed under a Creative Commons Attribution (CC BY) license (<http://creativecommons.org/licenses/by/4.0/>). <https://doi.org/10.1063/5.0120124>

## I. INTRODUCTION

Lifting surfaces are ubiquitous devices used across a wide range of industries and applications, including energy generation, transportation, and the built environment. Unfortunately, they can also be responsible for a large proportion of the noise generated in these sectors. Within the transport sector, lifting surface noise arises in many places, including from marine propellers,<sup>1</sup> aircraft wings and slats,<sup>2</sup> fan noise from turbofans,<sup>3</sup> and helicopter rotor noise.<sup>4</sup> Unmanned drones also produce significant levels of noise,<sup>5</sup> much of which is aerodynamic noise from the blades.<sup>6</sup> Within the energy sector, wind turbine noise is often cited as an issue and extensive research has been undertaken to improve blade design to reduce this. Lifting bodies can produce noise in a number of different ways, including trailing-edge noise, leading-edge noise, and tip vortex noise. Reviews and more detailed descriptions of these sources can be found in a number of works.<sup>7–9</sup> Trailing-edge noise, which is the focus of this study, occurs when the boundary layer (laminar, transitional, or turbulent) convects over the trailing edge. This is often the dominant source of aerodynamic noise on wind turbines<sup>10</sup> and so is a problem of great interest at present.

At low Reynolds numbers where the boundary layer is laminar, this typically produces a tonal noise due to vortex shedding, where the frequency is determined by the boundary layer thickness. For a turbulent boundary layer, the fluctuations in the boundary layer induce pressure fluctuations as they convect over the trailing edge, which scatter as acoustic waves. Depending on the character of the boundary layer and the trailing-edge geometry, the noise produced can either be narrow-band or broadband.

At moderate Reynolds numbers, typically  $O(10^4 - 10^5)$  based on chord length, tonal instability noise can occur. This happens when Tollmien–Schlichting (T–S) instability waves in the boundary layer are amplified upstream of the trailing edge, where they scatter as acoustic waves. These phenomena can occur on small aerial vehicles and wind turbines, where the noise is perceived as problematic.<sup>11</sup> Tonal instability noise has been extensively researched both experimentally<sup>12–16</sup> and numerically,<sup>17–21</sup> and this body of work has led to a good understanding of the underlying physical mechanisms of trailing-edge noise, although some questions remain around the exact role of a feedback mechanism and consistent and accurate predictions are still

challenging. The feedback hypothesis states that the instability waves in the boundary result from freestream fluctuations scattered at the trailing edge, which propagate upstream. These long-wave freestream fluctuations induce short-wave instability waves in the boundary layer, which then propagate downstream before scattering at the trailing edge, completing the loop. The system is therefore self-sustaining, with the trailing-edge flow determining the nature of the upstream fluctuations, which then in turn determines the trailing-edge flow. Instability noise can only occur if the boundary layer is transitional on at least one side of the airfoil, with a high degree of spanwise correlation. The amplification of the instability wave occurs just upstream of the trailing edge, and this requires a small region of separation to be present in the boundary layer.<sup>14,15</sup> If all of these conditions are met, high-amplitude tonal/narrowband noise will be produced.

A wide range of geometry modifications have been proposed for reducing the noise from airfoils. For reducing or eliminating trailing-edge instability noise, one of the most widely studied is the serrated trailing edge.<sup>22–27</sup> Serrated edges can be effective for both instability noise and trailing-edge noise from a turbulent boundary layer, and there are some similarities in the underlying mechanisms. For a turbulent boundary layer, the serrations can be effective at reducing noise across a wide frequency band, particularly at lower frequencies, which are associated with the larger turbulent structures within the boundary layer. The geometry of the serrations is important here. One experimental study<sup>24</sup> demonstrated that serrations with a wavelength associated with the Strouhal shedding frequency for a hydrodynamically blunt trailing edge were most effective. This study also found that the serrated edges do modify the underlying flow and that this is fundamental to the noise reduction. This assertion countered some previous works where it was assumed that the effect of the serrations was primarily on the acoustic field, and helped to demonstrate the importance of flow modification for trailing-edge noise reduction. Subsequent research has found that one of the primary mechanisms by which serrations work is breaking up the larger coherent structures, thus reducing the scattering efficiency. This applies to both instability noise, where a two-dimensional vortical structure is present, and also to turbulent boundary layers. Additionally, for a transitional boundary layer serrations can also prevent or reduce the separated region upstream of the trailing edge,<sup>22</sup> which prevents or at least reduces the amplification of the instability waves.

Porous edges and surfaces can also act to reduce the correlation of a transitional or turbulent boundary layer, as well as reducing the convection velocity inside the boundary layer, which is an important determining factor for the magnitude of the scattered acoustic waves. A range of studies have considered porous and porous-serrated edges,<sup>28–30</sup> and these have shown good reductions in noise levels for a range of conditions. However, the large reduction in the noise at the T–S frequency is partially offset by an increase in noise at higher frequencies, which has been attributed to friction between the porous surface and the flow.<sup>30</sup> Porous airfoils can also have higher drag than non-porous airfoils<sup>28</sup> and so this needs to be weighed against their noise reducing properties.

Inspired by natural geometries, Wang *et al.*<sup>31</sup> developed an airfoil incorporating serrated edges and surface ridges. Large-eddy simulations (LESs) were combined with an acoustic analogy to determine the effectiveness at reducing trailing-edge noise at  $Re = 1 \times 10^5$ . The results showed a reduction in noise of over 13 dB, with very little

change in the drag. Two mechanisms are suggested for this: a reduction in the velocity fluctuations immediately upstream of the trailing edge and a reduction in the spanwise correlation of the large-scale vortices that are associated with the high-amplitude tonal component of the noise. This type of geometry shows much promise, particularly noting the minimal impact on drag that was observed in this study. It is noted that surface ridges can be effective at reducing drag for fully turbulent boundary layers,<sup>32,33</sup> but this is for ridges that are perpendicular, rather than parallel to the flow.

Another geometry inspired by nature is the leading-edge tubercle, which is present on the fins of humpback whales. These were initially investigated as a means of delaying stall and improving performance at high angles of attack,<sup>34–36</sup> but they can also be very effective at reducing noise and a number of studies have considered the use of tubercles and leading-edge serrations for this.<sup>37–39</sup> It has been shown that wavy leading-edge serrations are more effective than straight serrations.<sup>40</sup> The wavy serrations were found to introduce a phase interference which, combined with the destructive effects of the geometric obliquity resulted in a superior acoustic performance. Modifications involving waves, grooves, or serrations tend to consist only of a single length-scale, whether that be the wavelength or the width of the serration. However, it was found in one study<sup>41</sup> that by using a double wavelength serration a better noise reduction could be achieved compared with a single wavelength. This was attributed to interference between adjacent sources at the leading edge. As with trailing-edge serrations and porous surfaces, leading edge serrations are generally associated with a reduction in aerodynamic performance at low to moderate angles of attack. In particular, there is an inverse relationship between noise reduction and drag, with increasing serration amplitude leading to improved noise performance but a reducing lift-to-drag ratio.<sup>39</sup>

The potential to reduce noise with no penalty in aerodynamic performance is the motivation behind the present study, which considers the use of wavy geometries for reducing trailing-edge noise at moderate Reynolds numbers. A wavy airfoil has a number of potential benefits. First, it shares some similarities with the surface ridges considered by Wang *et al.*<sup>31</sup> and so a wavy geometry should reduce the trailing-edge noise to some degree if designed appropriately. Second, if the freestream flow is turbulent there is the potential for the wavy surface to reduce the leading-edge noise produced by turbulence scattering at the leading edge, as demonstrated by Refs. 40 and 42. Wavy leading edges and wavy surfaces also share similarities with leading-edge tubercles in that they have been shown to improve aerodynamic performance at higher angles of attack.<sup>43</sup> Designed appropriately, a wavy lifting surface could be used in a wide range of applications, including wind turbines, marine propellers, and other areas where lifting body noise is problematic.

In this paper, the effect of spanwise wavy geometries on the aerodynamic properties and the trailing-edge noise of an airfoil is considered. Using large-eddy simulations (LES) coupled with an aeroacoustic model, the aerodynamic performance and trailing-edge noise of a NACA0012 (National Advisory Committee for Aeronautics) foil is compared with that from four variants, which incorporate span-wise surface waves. The first three variants have a spanwise wave with a single wavelength, whereas the fourth has a wave consisting of two sine waves of different wavelengths to create a more irregular variation in the surface geometry. The heights of the surface waves are small

relative to the geometry, at 4% of the maximum airfoil thickness as we wish to investigate whether or not a spanwise variation can be effective at reducing the noise without inducing a premature transition of the boundary layer. While this would reduce the noise due to turbulent boundary layers being less efficient acoustic sources than transitional ones,<sup>44</sup> it would also lead to a sharp increase in drag. The Reynolds number considered is  $Re = 64\,000$ , and the Mach number is  $Ma = 0.023$ . Each airfoil is modeled at an angle of attack of  $\alpha = 1^\circ$ , and the aerodynamic and aero-acoustic performance is assessed. The smooth airfoil and variant 4 are then considered over a range of angles:  $0^\circ \leq \alpha \leq 4^\circ$  to provide a broader assessment of the performance of this variant as compared to the smooth airfoil.

The hybrid aeroacoustic model<sup>45</sup> uses an incompressible fluid simulation to resolve the turbulent flow field, from which acoustic source terms are computed. The source terms are then interpolated onto a separate, partially overlapping grid where the acoustic perturbation equations are solved numerically. This approach is more efficient for low Mach number flows than a compressible simulation, but provides more detail than an acoustic analogy approach, and also removes the ambiguity of how to treat the source terms that often arises here. Despite being less widely used than an acoustic analogy approach or a compressible simulation, the hybrid method has been successfully applied to the study of trailing-edge noise by a number of researchers.<sup>30,45,46</sup> Verification and validation of the fluid and acoustic parts of the simulation are presented in Sec. III with the far-field acoustic pressure being compared to experimental data<sup>47</sup> to provide confidence in the methodology.

## II. METHODS

### A. Governing equations and numerical methods

The simulations conducted in this study are performed using a hybrid computational aero-acoustic code<sup>45</sup> where the fluid and acoustic fields are resolved on separate, partially overlapping domains. Incompressible large-eddy simulations are first solved in the fluid domain, from which acoustic source terms are computed and then interpolated onto a larger acoustic domain. The acoustic perturbation equations are then solved in the acoustic domain to obtain the three-dimensional acoustic pressure field. The coupling between the fluid and acoustic fields is one-way and so neglects the impact of the acoustic pressure on the fluid field. This is valid for low Mach number flows such as those considered in this study, as demonstrated in Ref. 45.

The spatially filtered continuity and momentum equations for an incompressible fluid are given in the following equations:

$$\frac{\partial \widehat{U}_i}{\partial x_i} = 0, \tag{1}$$

$$\frac{\partial \widehat{U}_j}{\partial t} + U_j \frac{\partial \widehat{U}_i}{\partial x_i} = -\frac{1}{\rho} \frac{\partial \widehat{p}}{\partial x_j} + \nu \frac{\partial^2 \widehat{U}_j}{\partial x_i \partial x_i} - \frac{\partial \tau_{ij}}{\partial x_i}, \tag{2}$$

where

$$\tau_{ij} = \widehat{U}_i \widehat{U}_j - \widehat{U}_i \widehat{U}_j. \tag{3}$$

The hat notation is used here to denote spatially filtered variables. The sub-filter scales are modeled using the dynamic  $k$  model,<sup>48</sup> which has been shown to be suitable for modeling transitional flows over wings.<sup>49,50</sup> The equations are solved using the finite-volume approach,

with a blended scheme being used to discretize the convective terms. The scheme is 75% central differencing, 25% linear upwind, which is more stable than a pure central differencing scheme and only introduces a small amount of dissipation into the solution.<sup>49</sup> The time derivatives are discretized using a three-point backward scheme.

The acoustic source terms, defined in Eq. (4), are interpolated from the fluid domain to the acoustic domain using radial basis function (RBF) interpolation

$$S = -\frac{\partial \widehat{p}}{\partial t} - \widehat{U}_i \frac{\partial \widehat{p}}{\partial x_i}. \tag{4}$$

This method interpolates the source terms to each acoustic cell using a cloud of points from the fluid domain that are close to the location of the acoustic cell. For a typical hexahedral mesh in three dimensions, 25 fluid cells are used for each interpolation. Using a scale-invariant multi-quadric basis function, this method is accurate and robust. Details of the method, together with accuracy and convergence characteristics can be found in Ref. 45.

The acoustic perturbation Eqs. (5) and (6) are a system of four hyperbolic equations for the acoustic pressure ( $p_a$ ) and velocity ( $u_a$ )

$$\frac{\partial p_a}{\partial t} + \overline{U}_i \frac{\partial p_a}{\partial x_i} + \rho_0 c_0^2 \frac{\partial u_{a_i}}{\partial x_i} = S, \tag{5}$$

$$\frac{\partial u_{a_i}}{\partial t} + \overline{U}_i \frac{\partial u_{a_i}}{\partial x_j} + \frac{1}{\rho_0} \frac{\partial p_a}{\partial x_i} = 0. \tag{6}$$

Here,  $\overline{U}_i$  denotes the mean fluid velocity, and  $c_0 = 343 \text{ ms}^{-1}$  and  $\rho_0 = 1.23 \text{ kg m}^{-3}$  denote the speed of sound and fluid density, respectively, and are assumed to be spatially invariant. For low Mach number problems such as those considered here, it is convenient to neglect the effect of the mean velocity. This has only a very small effect on the acoustic field at low Mach numbers and so can be neglected without any meaningful loss of accuracy. This improves the efficiency of the simulation and removes the need to interpolate source terms with high-velocity gradients close to the wall, which requires a higher resolution for the acoustic grid, further degrading the computational performance. As with the fluid equations, the acoustic perturbation equations are solved using the finite volume framework. The flux evaluation is performed using an exact Riemann solver with linear reconstruction, which ensures conservation and can be applied to unstructured grids with no restriction on cell type. The spatial discretization reduces the equations to a system of ordinary differential equations, which are solved using a third-order strong stability preserving Runge–Kutta scheme.

For a typical low Mach number problem, the time step for the acoustic solver will be smaller than for the fluid solver. For the cases considered here,  $Ma = 0.023$ , which requires 30 acoustic time-steps per fluid time-step. The Courant number for both parts of the simulation is  $C < 1.0$ .

The method is implemented within OpenFOAM. Both parts are solved simultaneously and in parallel, which reduces the computational time and memory requirements.

### B. Geometry and meshing

The airfoil geometries used in this study are based on the NACA0012 airfoil. Each foil has a nominal chord length of  $c = 0.12 \text{ m}$

and a span of  $s = 0.06$  m. The trailing edge of each foil has been rounded to accommodate the modifications to the surface geometry, resulting in a physical chord length of 0.114 m. This is shown in Fig. 1. Despite this reducing the sharpness of the trailing edge, it will be shown in Sec. III that the edge is neither hydrodynamically nor acoustically blunt. Specifically, the boundary layer is thicker than the trailing edge, and the acoustic field will be shown to result from the instability waves in the boundary layer rather than vortex shedding associated with a Strouhal shedding frequency.

Alongside an airfoil with the usual NACA0012 profile, four variations are considered, which have a spanwise wavy surface (Fig. 2). The wavy geometry is uniform along the chord length and is designed such that the mean thickness of the foil remains the same as the original NACA0012 foil. The wavy surface for the first three variants consists of a single sine wave with a height of  $h = 0.04t_{\max}/c$  and wavelengths of  $\lambda/c = 0.25, 0.1, 0.05$ , respectively.  $t_{\max}$  denotes the maximum thickness, as determined by the usual NACA0012 profile. The fourth variant has a surface modified by adding two waves together: both with a height of  $h = 0.02t_{\max}/c$  and wavelengths of  $\lambda/c = 0.1, 0.0625$ . These wavelengths were chosen to create a more irregular surface variation while maintaining spanwise periodicity. The change in surface area of the variants is small: increasing by less than 1% for variants 1, 2, and 4, and by 2% for variant 3. The four variants are shown in 2 together with the spanwise variation in the surface compared with the smooth airfoil.

A dual-domain approach is used with the hybrid model with partially overlapping grids, and this is illustrated in Fig. 3. The fluid domain extends three chord-lengths upstream of the geometry and ten lengths downstream. The airfoil is pinned at either side by periodic boundaries. The fluid mesh is block-structured and consists of hexahedral cells. The resolution is based on the sensitivity studies carried out in Ref. 49 with an additional level of spanwise refinement to ensure that the three-dimensional flow resulting from the surface geometry is adequately resolved. The non-dimensional near-wall grid resolution satisfies  $\zeta^+ < 10$ ,  $\eta^+ < 1$ , and  $z^+ < 12$ , where  $\zeta$ ,  $\eta$ ,  $z$  denote the chordwise, wall-normal, and spanwise directions, respectively. The total number of cells for the fluid mesh is 30 480 000.

The acoustic domain is designed to allow for the acoustic waves to propagate spherically and so the geometry is not pinned at the sides but is located in the middle of a  $4 \times 4 \times 4$  m<sup>3</sup> domain. The acoustic mesh is hex-dominant and is refined in the acoustic source region around the foil and also up to 1.5 m away from the airfoil in all directions to allow for the waves to propagate without artificial dissipation. Verification studies presented in Ref. 45 showed that around 30 cells per wavelength are needed for this, and the grid used has a resolution of 0.01 m. This means that acoustic waves with frequencies up to 1150 Hz should be fully resolved. The experimental data,<sup>47</sup> against which simulations of the smooth airfoil are compared in Sec. III A

showed that the dominant frequency was approximately 300 Hz. The mesh is coarsened toward the far-field boundaries, and a perfectly matched layer is used to attenuate the waves close to the boundaries and prevent unwanted wave reflections. This technique is commonly used in simulations of wave propagation problems<sup>45,51</sup> and works by modifying the governing equations in the complex domain to attenuate waves before they reach the boundaries.

### III. RESULTS AND DISCUSSION

#### A. Verification and validation

To provide confidence in the subsequent results and analysis, data for the smooth airfoil have been compared to a number of sources for  $\alpha = 1^\circ$ . First, the mean pressure over the chord is shown in Fig. 4, with the data compared to results from XFOIL<sup>52</sup> using viscous analysis at  $Re = 64\,000$ . The same geometry was imported into XFOIL to provide a more accurate comparison, and excellent agreement is seen between the simulation and XFOIL, as shown in Fig. 4. The mean drag coefficient predicted by the large-eddy simulation is  $\bar{C}_D = 0.0237$  compared to  $\bar{C}_D = 0.0223$  from XFOIL. Both the simulation and XFOIL predict similar contributions in terms of frictional and pressure drag, with  $\bar{C}_{D_f} = 0.0098$  from the simulation and  $\bar{C}_{D_f} = 0.0093$  from XFOIL. The mean lift coefficient predicted by the LES is  $\bar{C}_L = 0.002$ , which compares with  $\bar{C}_L = 0.001$  from XFOIL. The reason for this very small value, despite the non-zero angle of attack, is the Reynolds number. Analysis using XFOIL has shown that the lift coefficient at  $\alpha = 1^\circ$  is very small for  $Re \leq 64\,000$  but increases for higher Reynolds numbers.

The far-field acoustic spectra can be compared to the experimental data of Yakhina *et al.*<sup>47</sup> These experiments were carried using a NACA0012 airfoil at the same Reynolds and Mach number. The acoustic pressure was recorded at a location 1.5 m above the airfoil. As the span used in the experiment was five times greater than that used in the simulations, it is necessary to scale the data from the simulation. The spanwise correlation reported in the experiments was high with the flow over the wing surface being described as effectively two-dimensional. This has also shown for this configuration numerically.<sup>45</sup> From this, it can be inferred that the spanwise correlation length is greater than the span used in the experiment, and so we can use the following formula to scale the sound pressure levels from the simulation:<sup>53</sup>

$$SPL_e = SPL_s + 20 \log_{10} \left( \frac{S_e}{S_s} \right), \quad (7)$$

where  $S_e$  denotes the experimental span and  $S_s$  denotes the simulated span. The sound pressure levels can also be compared to the results presented by Smith and Ventikos.<sup>45</sup> These were also large-eddy

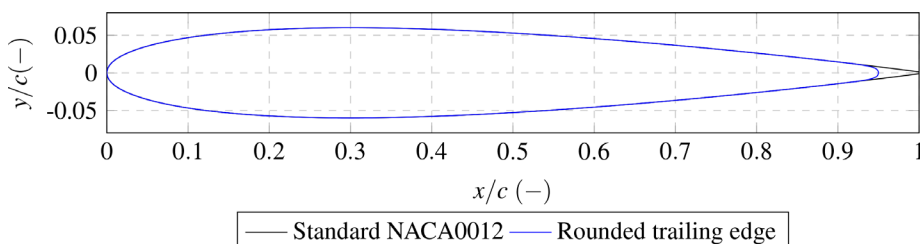
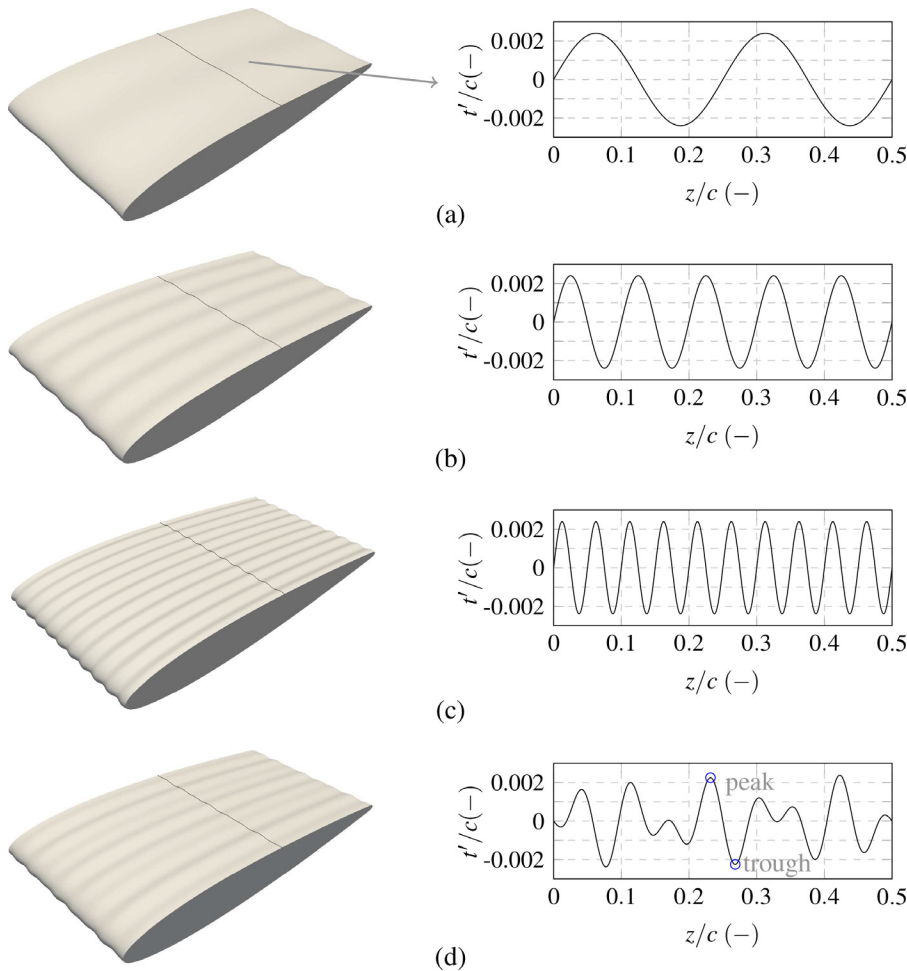
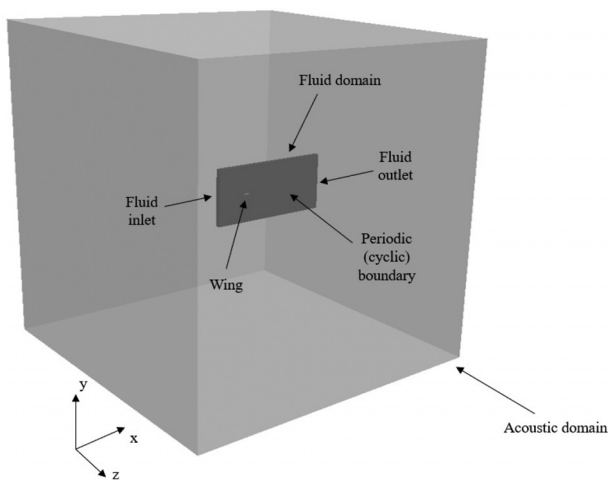


FIG. 1. Airfoil profiles for the standard NACA0012 and the rounded trailing edge used in this study.



**FIG. 2.** Illustration of the 3D geometry for variants (a) 1, (b) 2, (c) 3, and (d) 4 together with the spanwise variation relative to the baseline NACA0012 airfoil. The specific locations peak and trough used in subsequent analysis are shown for variant 4.



**FIG. 3.** Illustration of the fluid (dark gray) and acoustic (light gray) domains used for the simulation. The origin for both domains is at the right-hand side of the leading edge of the airfoil.

simulations conducted with a similar mesh resolution, but at the same span as the experiments. The results in Fig. 5 show good overall agreement, although the simulation over-predicts both the frequency and the amplitude of the narrowband component following scaling. It is interesting to note that this over-prediction was not seen for the simulation carried out at the same span as the experiment, suggesting that effects related to the span, or possibly the formula given in Eq. (7), are the cause of this. It is also possible that the geometry modification is playing a role here. The exact trailing-edge geometry used in the experiment is not known and so may differ slightly from that used in this work. Despite these differences, the comparison is generally good, with the drag coefficient, chordwise pressure distribution, and the acoustic far field being well predicted.

**B. Mean flow characteristics**

In this section, the mean flow characteristics are presented beginning with the lift, drag, and surface pressure each variant. Variants 3 and 4 are found to exhibit the largest change when compared with the smooth airfoil, and these have very similar mean flow characteristics. More detailed analysis is therefore presented for variant 3 to better

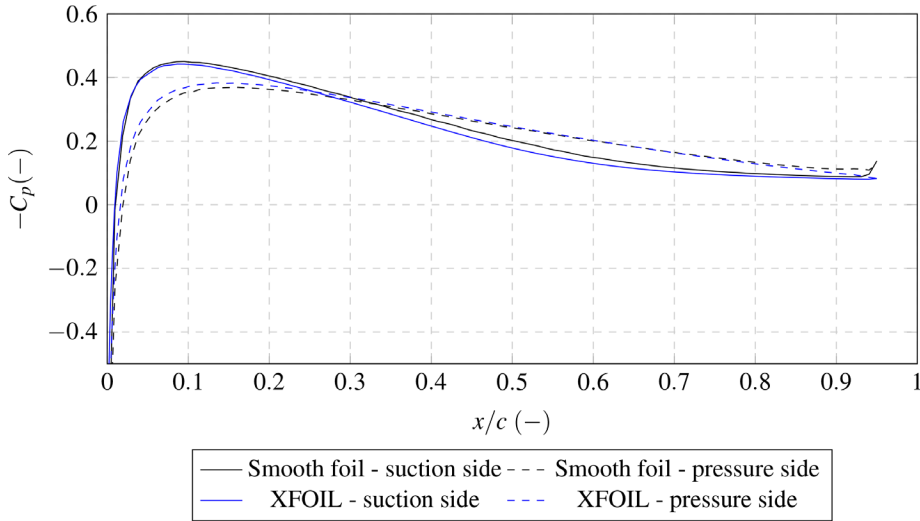


FIG. 4. Mean chordwise pressure over the smooth airfoil.

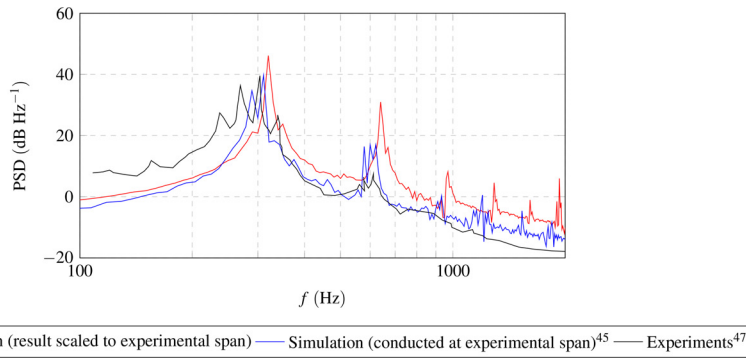


FIG. 5. Power spectral density of the sound pressure level at  $Re = 64\,000$ ,  $p_{ref} = 2 \times 10^{-5}$  Pa, plotted with simulations carried out at the experimental scale<sup>45</sup> and experimental results.<sup>47</sup>

understand the changes in shear stress and the boundary layer and how this affects the drag.

The mean lift and drag of the smooth airfoil together with the four variants is given in Table I. For consistency and in line with common practice, the lift and drag are non-dimensionalized using the chord and span as opposed to the surface area

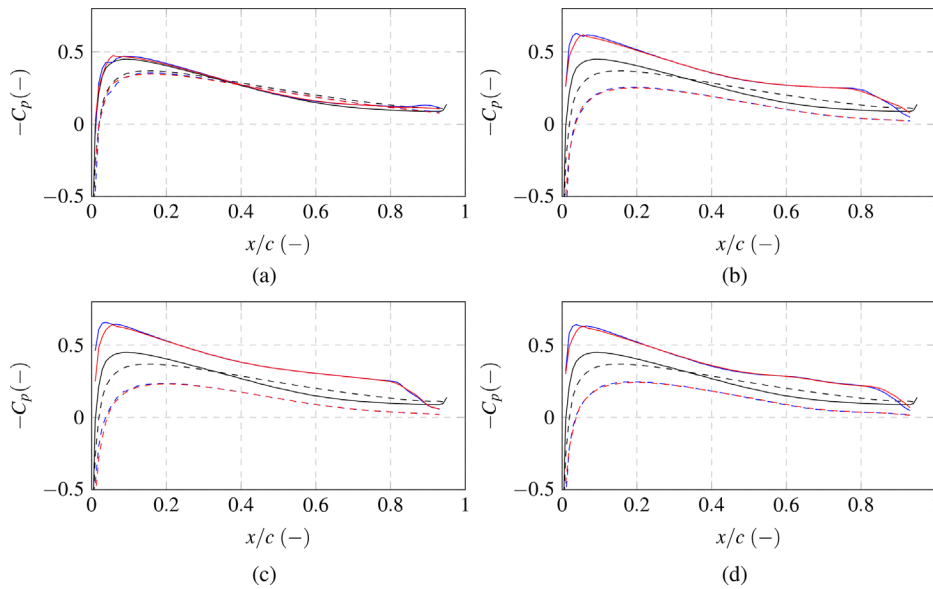
$$\bar{C}_{L,D} = \frac{\bar{F}_{L,D}}{\frac{1}{2} \rho c s U_\infty^2}. \quad (8)$$

TABLE I. Mean lift and drag of the five airfoils at  $\alpha = 1^\circ$ . The drag coefficient is also shown split into the relative contributions from frictional and pressure drag.

| Wing      | $\bar{C}_L$ | $\bar{C}_D$ | $\bar{C}_{D_f}/\bar{C}_D$ | $\bar{C}_{D_p}/\bar{C}_D$ |
|-----------|-------------|-------------|---------------------------|---------------------------|
| Smooth    | 0.002       | 0.024       | 0.41                      | 0.59                      |
| Variant 1 | 0.037       | 0.024       | 0.40                      | 0.60                      |
| Variant 2 | 0.227       | 0.023       | 0.41                      | 0.59                      |
| Variant 3 | 0.259       | 0.023       | 0.39                      | 0.61                      |
| Variant 4 | 0.240       | 0.022       | 0.39                      | 0.61                      |

The drag coefficient remains unchanged for variant 1, but is lower for 2 and 3, and lower still for variant 4, with an 8% reduction compared to the smooth airfoil. For variants 3 and 4, the majority of the drag reduction is due to a reduction in the frictional component, but there is also a small decrease in the pressure drag. The lift coefficient of the smooth foil is very small, and this has been attributed to the trailing-edge geometry. If the same geometry is modeled in XFOIL, a lift coefficient of close to zero is also predicted, and this is lower than that for the same geometry with a sharp trailing edge. As with the drag, the lift of variant 1 is similar to that of the smooth foil, implying that the longer surface waves are having only a limited impact on the mean aerodynamic performance. For variants 2–4, a significant increase in the lift is observed. To confirm that the variants remain symmetric about mid-chord and that no net camber has been introduced by the geometry modifications, a simulation has been run at  $\alpha = -1^\circ$  and the surface pressure coefficients have been compared. The results of this have confirmed this symmetry, with the pressure on the upper surface for  $\alpha = -1^\circ$  matching the pressure on the lower surface for  $\alpha = 1^\circ$  and vice versa.

Insight into the change in lift can be gained by considering the mean chordwise pressure distribution over the foil. This is shown for each variant together with the pressure distribution for the smooth



**FIG. 6.** Mean pressure coefficient over the chord. The black line denotes the smooth airfoil. The blue lines denote the pressure in a trough for variants 1–4, and the red lines denote the pressure along a peak. Solid lines represent the suction side, and dashed lines represent the pressure side. (a) Variant 1, (b) variant 2, (c) variant 3, and (d) variant 4.

airfoil in Fig. 6. For variant 1, the pressure distribution is almost unchanged from the smooth airfoil, which explains why the lift coefficient remains low. Variants 2–4 exhibit different behavior to this, with the pressure dropping more over the suction side and less over the pressure side. This explains the changes in lift reported in Table I, as there is a larger pressure differential between the two sides. Interestingly, there is very little difference between the mean pressures in a trough compared with a peak. In fact, the mean pressure distribution remains roughly constant across the entire span.

The pressure changes are the result of changes in flow velocity over the foil, rather than flow separation. For variants 2–4, the flow accelerates more over the suction-side leading edge, but less than for the smooth airfoil on the pressure side. This is confirmed by looking at the mean boundary layer profiles at  $x/c = 0.3$ , which is the location of maximum thickness for all variants. These are shown in Fig. 7 for the smooth airfoil and variant 3. On the pressure side, the mean tangential velocity just outside of the boundary layer is  $U_\zeta/U_\infty = 1.15$  for the smooth airfoil and 1.09 for variant 3. The non-dimensional velocity on the suction side is 1.15 for the smooth airfoil but increases to 1.19 for variant 3. This explains the changes observed in the surface pressures and the lift coefficients shown earlier.

As well as showing the velocity changes at the edge of the boundary layer, Fig. 7 also shows that the boundary layer thickness increases

in a trough but decreases in a peak. The mean effect is an increase in the overall thickness, which would usually lead to an increase in drag. However, this is not the case, and the drag decreases for variant 3 compared to the smooth airfoil. To understand this, we must consider how both the boundary layer and the shear force change along the chord length. The displacement thickness,<sup>54</sup>  $\delta^*$ , is a useful measure in this regard as it can help explain the changes in pressure drag that occur at the trailing edge. This is a measure of the mass deficit within the boundary layer, which translates into a pressure drop downstream of the trailing edge. Thus, a larger displacement thickness at the trailing edge will lead to an increase in the pressure drag. The displacement thickness is calculated using

$$\delta^* = \int_0^\delta \left(1 - \frac{U_\zeta}{U_\infty}\right) d\eta. \tag{9}$$

This is shown in Fig. 8, again for the smooth airfoil and variant 3. For the smooth airfoil, the growth is as one would expect. The growth on the pressure side is restricted due to the positive pressure gradient that results from the angle of attack of the foil. On the suction side, the growth is much larger owing to the adverse pressure gradient that results from both the angle of attack and the tapering of the airfoil toward the trailing edge. It is useful to consider this alongside the

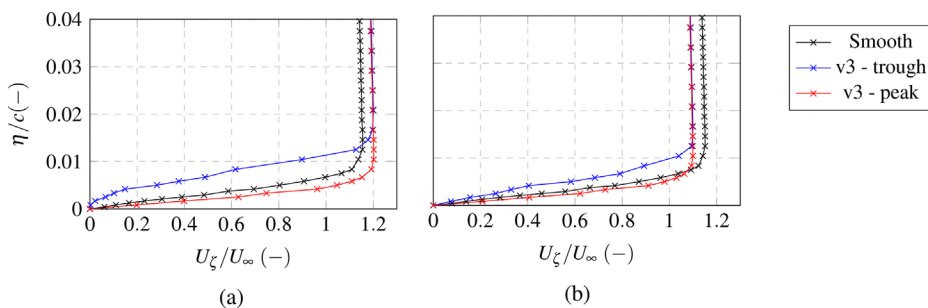


**FIG. 7.** Mean tangential velocity close to the wall at  $x/c = 0.3$  for the smooth airfoil and variant 3 in a peak and a trough on (a) suction side and (b) pressure side.



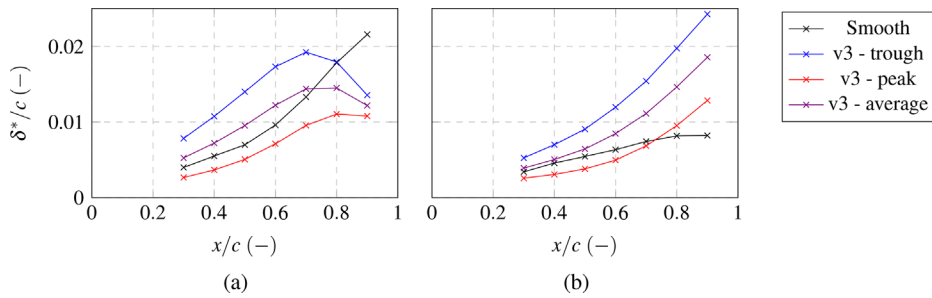


FIG. 8. Displacement thickness of the boundary layer on (a) suction side and (b) pressure side for the smooth airfoil and variant 3.

mean shear stress on the surface, which is shown in Fig. 9. The flow on the suction side of the smooth airfoil separates at approximately  $x/c = 0.6$ , corresponding to the change in sign of the shear stress. This separation coincides with a more rapid growth in the boundary layer thickness. On the pressure side, the boundary layer remains attached along the entire chord length.

For variant 3, the picture is somewhat different both in terms of the boundary layer thickness and the shear stress. On the suction side, the boundary layer in the troughs separates at  $x/c = 0.3$  but remains attached along the peaks. Despite the local variations, the span-wise averaged shear is very similar to that of the smooth airfoil over the suction side. The same is true on the pressure side over the first half of the chord, but this changes downstream of mid-chord. Here, the flow in the troughs separates, leading to reversed flow close to the wall. This leads to a net reduction in the shear stress on the pressure side when compared to the smooth airfoil. As one would expect, this does increase the boundary layer thickness on the pressure side, as shown in Fig. 8, and this would normally be associated with an increase in the pressure drag. However, this is not the case, and the pressure drag actually decreases slightly for this case. This can be explained by noting that the suction side boundary layer thickness decreases toward the trailing edge. This results in the combined thickness of the pressure and suction side boundary layers being similar for the smooth airfoil and variant 3.

These changes can also be seen in the velocity contour plots in Fig. 10. On the suction side of the smooth airfoil, the growth of the boundary layer can be seen together with the reversed flow toward the trailing edge. For variant 3, the thickness is higher over much of the suction side in the troughs and reversed flow exists over much of the chord length. However, toward the trailing edge, the boundary layer does not continue to grow and instead becomes thinner. This is due to the development vortices in the boundary layer, which lead to the flow becoming more attached. The development of these structures

and their effect on the flow is discussed in more detail in Sec. III C. On the pressure side of variant 3, the reversed flow is clearly present in the troughs, but not at the peaks, where the flow remains attached along the chord length. The changes in the boundary layer upstream of the trailing edge alter the pressure field immediately downstream of it, as shown in Fig. 11. This shows that the pressure deficit in the near wake is less for variant 3 than for the smooth wing, which helps to explain how the overall pressure drag decreases.

Taking all of these effects together, the drag force is lower because of a reduction in the shear stress due to the separation in the troughs on the pressure side, and also a smaller reduction in the pressure drag due to the changes in the suction-side boundary layer toward the trailing edge. This also shows that the drag reduction is not due to a change in the bluntness at the trailing edge that was introduced in order to add the surface waves. While this has rendered the trailing edge less sharp than the standard NACA0012 foil, the thickness is still less than that of the boundary layer at the trailing edge [as can be seen in Fig. 10(a)], and it is the boundary layer that is modified by surface waves leading to the reduction in the pressure drag in the near-wake.

### C. Acoustic performance and unsteady flow analysis

For an airfoil operating in a uniform flow at a low angle of attack, the acoustic far-field is the result of the boundary layer convecting over the trailing edge, where it induces pressure fluctuations over the surface of the foil. To understand how the noise changes between the different cases, it is useful to work backwards from the far-field noise to the underlying fluid dynamics that create it. To begin with, Fig. 12 shows the three-dimensional acoustic field for each geometry, with iso-surfaces representing 30, 40, and 50 dB. It should be noted that the results here are not scaled as was done in Sec. III A. This was done solely for validation and would not be appropriate here because assumptions around spanwise correlation do not hold for all variants.

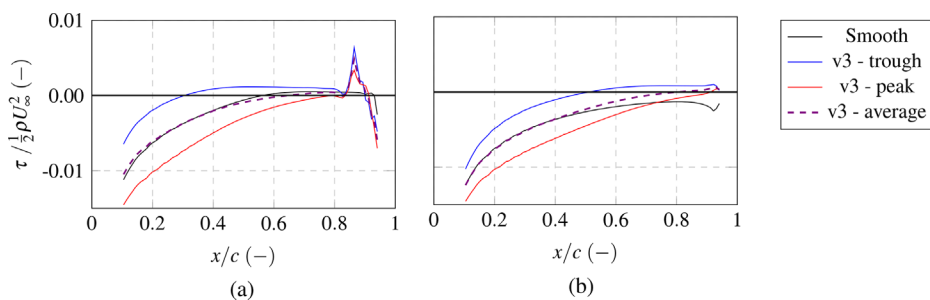


FIG. 9. Mean shear stress on (a) suction side and (b) pressure side for the smooth airfoil and variant 3.

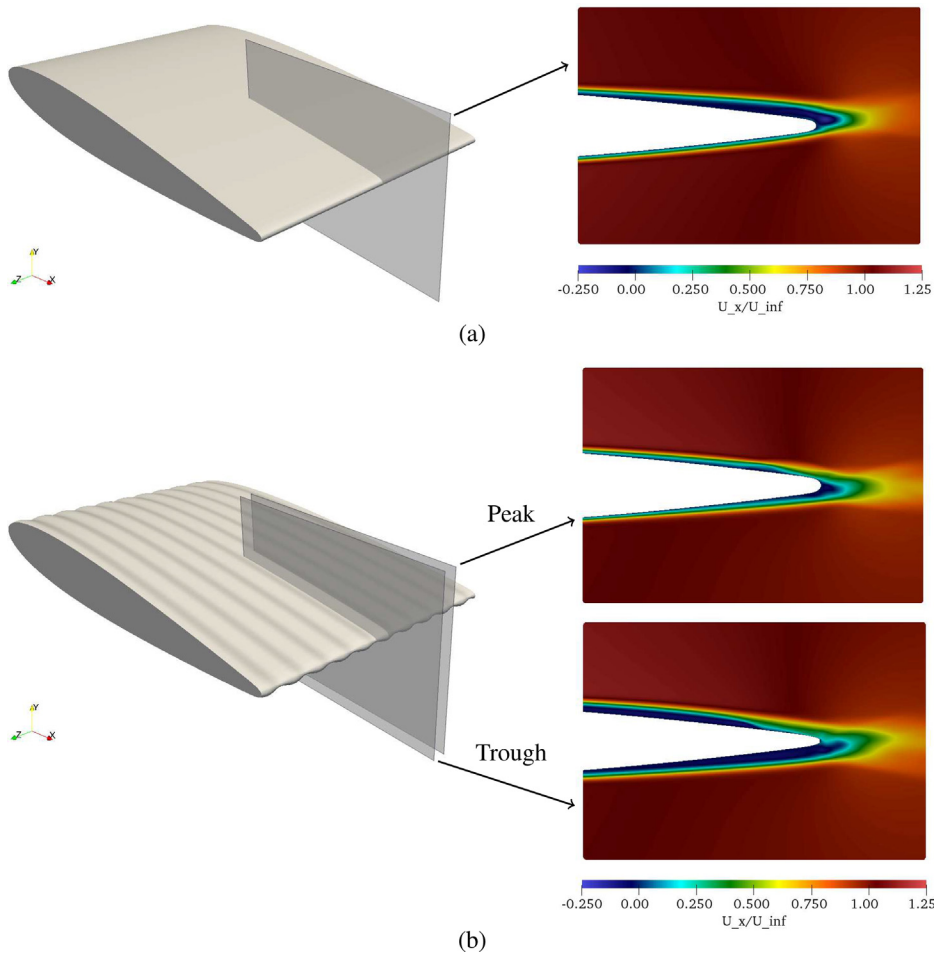


FIG. 10. Mean velocity contours over the trailing edge of (a) smooth airfoil and (b) variant 3. Contour plots are shown for both a peak and a trough for variant 3.

The acoustic field has the expected dipole pattern in all cases, with higher intensities directly above and below the airfoil, and lower intensities upstream and downstream. It should be noted that the 30 dB iso-contour is affected by the perfectly matched layer, which starts to attenuate the acoustic waves at  $r = 1.6$  m from the wing. This is most apparent for the smooth wing, where the 30 dB iso-contour is the furthest from the wing. For the smooth wing, the overall sound

pressure level is 39.7 dB for the reference point of (0.06, 1.5, 0.03), which corresponds to 1.5 m above the wing at mid-chord and mid-span. Variants 1 and 2 exhibit similar sound levels: 35.7 and 35.5 dB, respectively, representing a 4.0 and 4.2 dB reduction, respectively, when compared with the smooth wing. The acoustic field for variant 3 shows a smaller reduction than variants 1 and 2, with an overall sound pressure level (SPL) of 36.6 dB at the reference location for this variant,

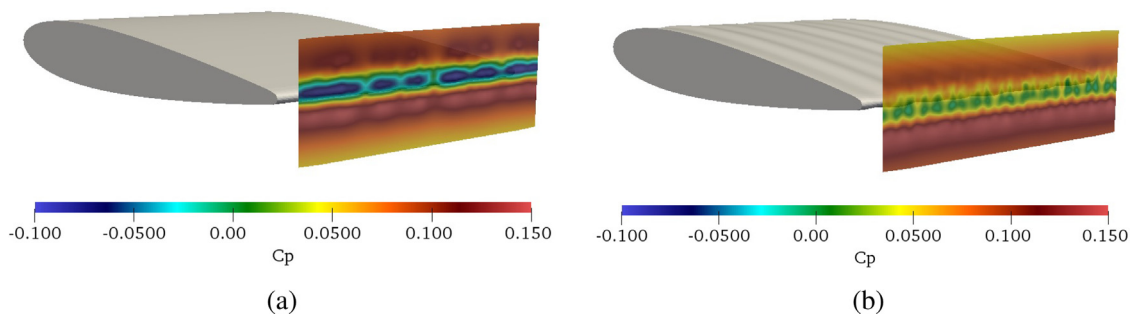
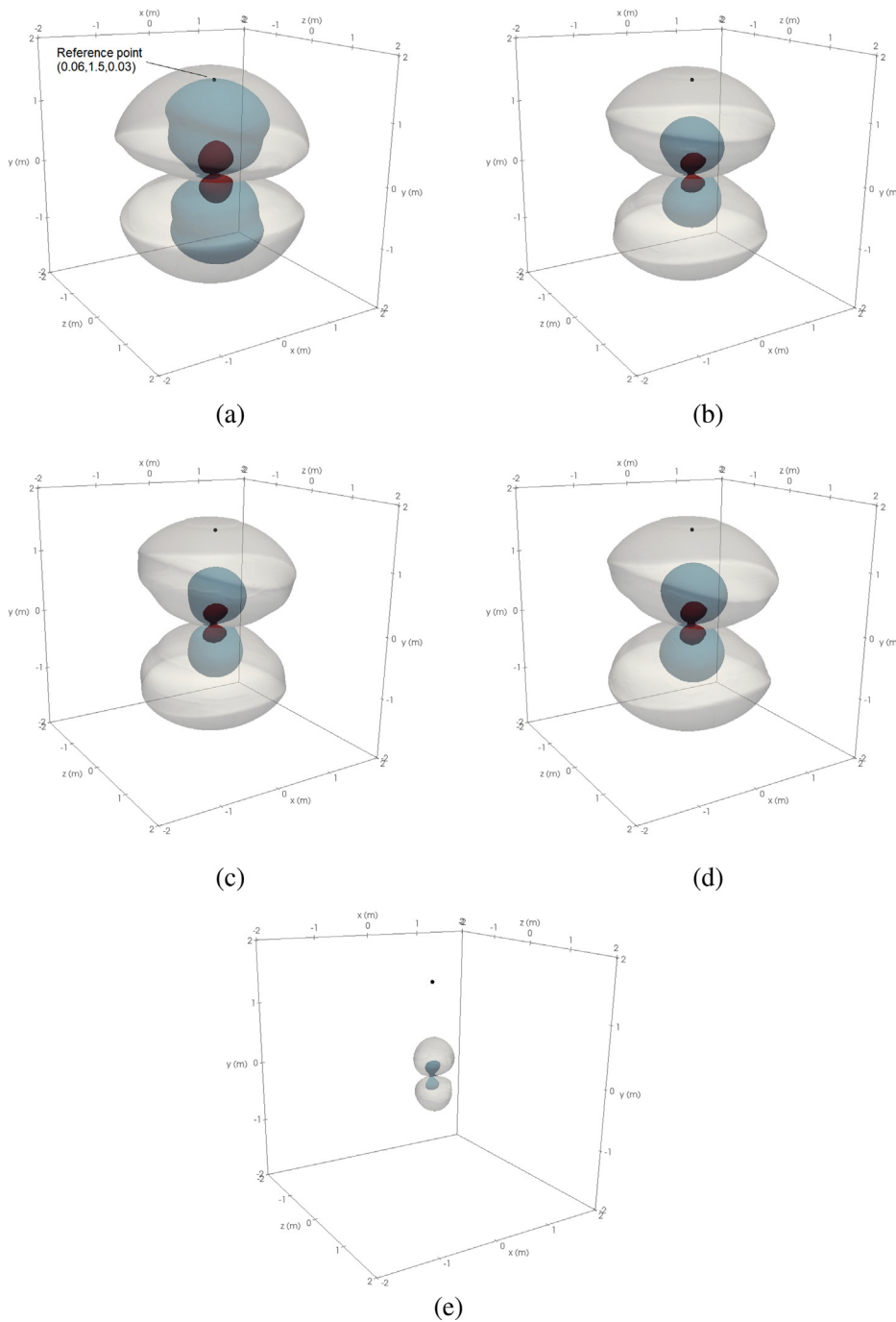


FIG. 11. Mean pressure coefficient downstream of the trailing edge for (a) smooth airfoil, and (b) variant 3.



**FIG. 12.** Acoustic field for (a) smooth, (b) variant 1, (c) variant 2, (d) variant 3, and (e) variant 4. Iso-surfaces are shown for overall sound pressure levels of 30 (gray), 40 (blue), and 50 dB (red).

but the acoustic field looks very similar to variants 1 and 2. For variant 4, a significant reduction is seen throughout the domain, with the overall SPL being 17.7 dB lower at the reference point. This suggests that a fundamental change in the nature of the flow over the wing has taken place for this case, even when compared to variants 1 to 3.

This is confirmed when considering the frequency content of the noise, as shown in Fig. 13. Again, this shows that the acoustic field is

similar for variants 1–3 but substantially different for variant 4. The spectra for variants 1–3 are dominated by a narrowband component similar to that seen for the smooth wing, but the peak amplitude is lower and secondary tones are evident. For variant 3, there is an increase in higher frequency noise, suggesting that the smaller spanwise waves are leading to higher frequency fluctuations at the trailing edge alongside those at the T-S frequency. For variant 4, the

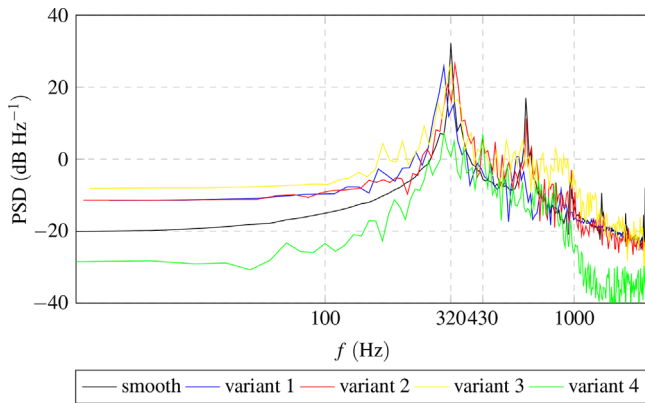


**FIG. 13.** Sound pressure level at the reference point for smooth wing and four variants.

narrowband component has largely disappeared, although there is still a broadband hump with tones at 300 and 430 Hz. The amplitudes are substantially lower over the frequency range where the T-S waves would be expected, again indicating a fundamental change in the boundary layer dynamics for this variant.

As discussed in the introduction, high-amplitude trailing-edge instability noise occurs when certain conditions are met: the boundary layer must be transitional on at least one side, there must be a small separated region on that side in which the amplification takes place, and there must also be a high level of spanwise correlation in the flow. The subsequent analysis therefore focusses on how these change for the different variants. Figure 14 shows iso-Q contours for the smooth wing and each variant, providing a snapshot of the vortical structures that form over the wing and in the near wake. For the smooth wing, tubular vortices can be seen toward the trailing edge on the suction side. These two-dimensional structures are typical of trailing-edge instability noise and explain why the acoustic field is dominated by a single frequency. For variants 1–3, the flow is still transitional and although it does exhibit a degree of three-dimensionality, the flow still has a high level of spanwise correlation, particularly for variant 3. Indeed, there is a clear spanwise periodicity the flow, with the spanwise length-scale being the wavelength of the surface geometry. This helps to explain why the noise reduction is only modest for these cases, as the surface waves are not altering the flow sufficiently enough to break up the dominant vortices associated with the boundary layer instability wave, or prevent their formation within the boundary layer.

The flow over the suction side of variant 4 is more three-dimensional than for the other cases, and appears much less structured. However, the flow structures are large and are not indicative of the boundary layer having transitioned fully to turbulence. As with the other variants, the flow does not transition to turbulence until downstream of the trailing edge. These dynamics are also shown in the left-hand panes of Fig. 15(a) (Multimedia view) for the smooth airfoil, Fig. 15(b) (Multimedia view) for variant 3, and Fig. 15(c) (Multimedia view) for variant 4. Here, the development and convection of the vortices in the boundary layer and near wake is illustrated using the iso-Q contours, alongside the acoustic source terms in the top-right pane and the acoustic pressure at midspan in the bottom-right pane. This highlights the similarities between the boundary layer flow for the

smooth airfoil and variant 3, and the notable differences for variant 4, both in terms of the spanwise correlation and the chordwise dynamics of the boundary layer.

The correlation coefficient  $R_z$  of the surface pressure between two points at a chordwise location of  $x/c = 0.9$ , separated by a spanwise distance  $d = z_2 - z_1$ , is given in Fig. 16 for both sides each wing. This is calculated using

$$R_z = \frac{\overline{p(z_1, t)p(z_2, t)}}{\sqrt{\left(\frac{1}{N} \sum_{j=1}^N (p(z_1, t_j) - \overline{p(z_1, t)})^2\right) \left(\frac{1}{N} \sum_{j=1}^N (p(z_2, t_j) - \overline{p(z_2, t)})^2\right)}} \quad (10)$$

The overbar notation is used to denote the mean over  $N$  time-steps, which corresponds to 10 chord-flow times.  $z_1$  is fixed, and due to the periodicity of the simulation, the maximum separation is  $d/s = 0.5$ . As expected, for the smooth wing the coefficient is high and does not decrease with distance. For the wavy wings, the correlation coefficient varies across the span, but is not a decreasing function of distance on the suction side. A clear periodicity can be seen which aligns with the geometric periodicity of each variant. This is most apparent for variant 3. The correlation coefficient has been computed here using a location in a trough as the first point. Distances of  $d/s = 0.1, 0.2, 0.3, 0.4, 0.5$  represent trough-to-trough correlation and it is clear that the correlation here is very high and that it decreases slightly for trough-to-peak,  $d/s = 0.15, 0.25, 0.35, 0.45$ . Similar behavior is observed for variants 1 and 2. The spanwise correlation is much higher on the pressure side, indicating that the higher pressure and is reducing the effects of the geometry on the spanwise variability of the flow. For variant 4, the correlation coefficients are lower, but they do not show a monotonic decrease with increasing distance, at least on the suction side, and again indicate a level of periodicity. The pressure side correlation decreases initially before stabilizing at around 0.7. No clear trend emerges here, and it may be that a simulation with a much longer span would be needed to identify whether there is any clear spanwise periodicity related to the periodicity of the surface geometry.

While these results help to qualitatively explain the acoustic data presented earlier, they do not give the complete picture. Variants 1–3 all exhibit a similar reduction in noise but have different levels of spanwise correlation. Furthermore, the reduction in the spanwise correlation for variant 4 does not explain the dramatic reduction in the noise produced by the trailing-edge flow. Therefore, as well as the spanwise correlation of the flow, we must also consider the dynamics of the boundary layer and the transition process in order to fully understand the acoustic performance of each wing.

The growth of the velocity fluctuations in the boundary layer is illustrated in Fig. 17 for the smooth wing and for variants 3 and 4. This is presented in the form of the thickness-averaged root mean square tangential velocity in the boundary layer at a particular chordwise position, calculated using

$$\hat{u}_\zeta = \frac{1}{U_\infty \delta} \int_0^\delta \sqrt{\frac{1}{N} \sum_{j=1}^N (U_{\zeta_j}(\eta) - \overline{U_\zeta(\eta)})^2} d\eta, \quad (11)$$

where the tangential velocities  $U_\zeta$  are considered over  $N$  time-steps, which corresponds to 10 chord-flow times. For variants 3 and 4, the

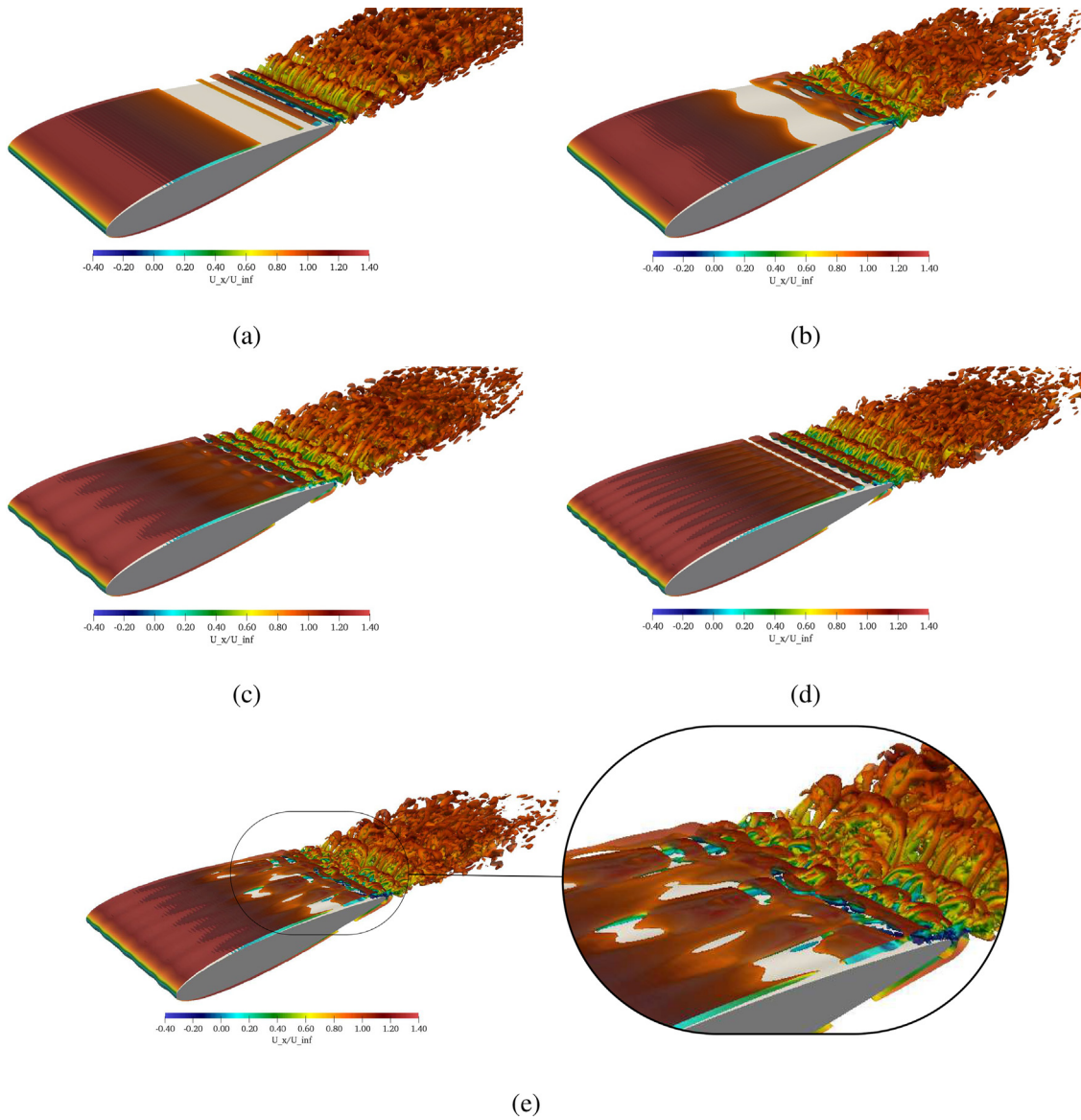


FIG. 14. Iso-Q contours ( $Q = 2 \times 10^4$ ) for (a) smooth airfoil, (b) variant 1, (c) variant 2, (d) variant 3, and (e) variant 4.

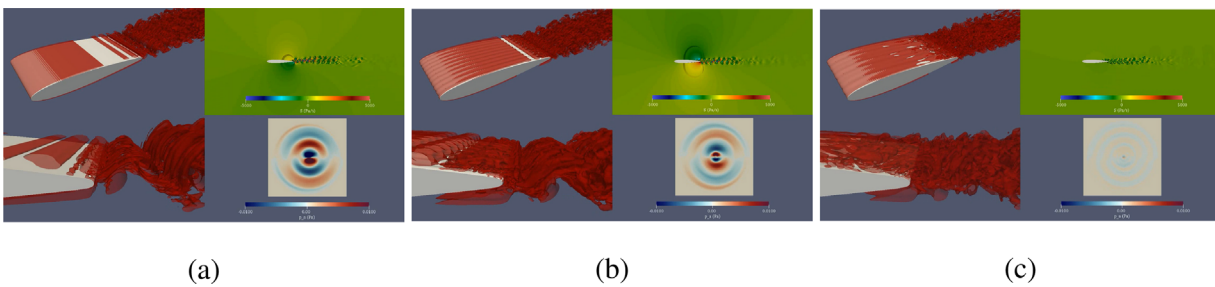


FIG. 15. Animations for (a) the smooth airfoil, and variants (b) 3, and (c) 4. The left-hand panes show iso-Q contours over the surface and at the trailing edge. The top-right pane shows the acoustic source terms, and the bottom-right pane shows the acoustic pressure at mid-span. The animations show the flow over 2 chord-flow times. Multimedia views: <https://doi.org/10.1063/5.0120124.1>; <https://doi.org/10.1063/5.0120124.2>; <https://doi.org/10.1063/5.0120124.3>

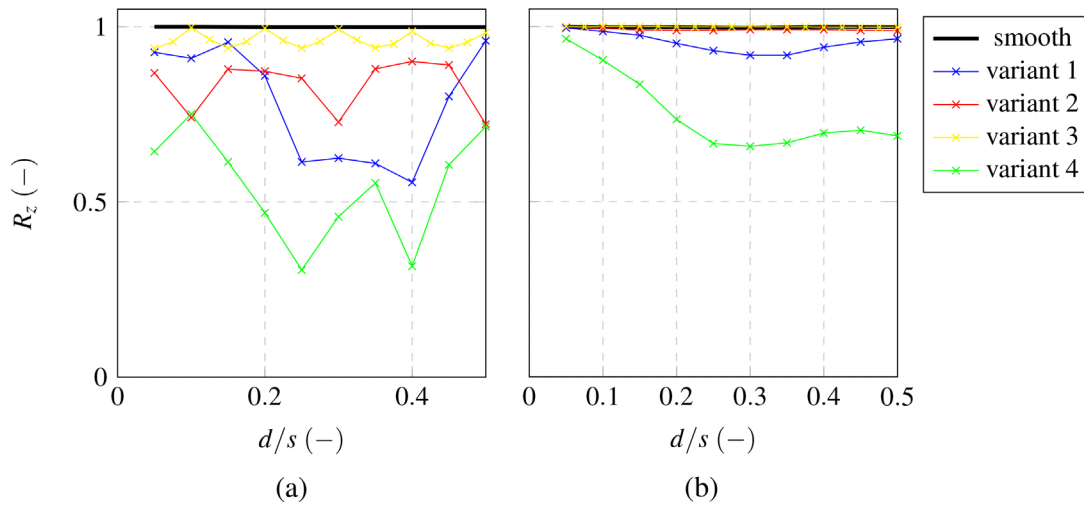


FIG. 16. Spanwise correlation coefficient for the surface pressure at  $x/c = 0.9$ . (a) Suction side, (b) pressure side.

fluctuations have been obtained for a peak and a trough. This measure is chosen over using a single location in the boundary layer because it accounts for any differences in the distribution of the fluctuations in the boundary layer, or for differences between the peaks and troughs. Comparing variant 3 with the smooth wing, it can be seen that the suction-side fluctuations are significantly higher along most of the chord, whereas those on the pressure side are similar. Upstream of  $x/c = 0.7$ , the fluctuations in the trough are higher than in the peak, but the values are similar downstream of this point. On the pressure side, there is little difference between the fluctuations in the peak and trough, and they are smaller than for the smooth wing here. This can be explained by noting that the pressure gradient was more favorable on the pressure side for variant 3 than the smooth wing, which inhibits the growth of boundary layer instabilities. For variant 4, the behavior is somewhat different. On the suction side, the fluctuations are again significantly higher, but unlike variant 3, they are an order of magnitude higher at  $x/c = 0.3$ . For variant 3, the growth accelerates downstream of  $x/c = 0.6$ , which is the same as for the smooth wing, but for variant 4 a two-stage growth pattern is observed, where the fluctuations stabilize at  $0.6 \leq x/c \leq 0.7$  before increasing significantly toward the trailing edge. On the pressure side, the fluctuations are also much higher upstream than for the smooth wing of variant 3, and

their growth actually slows toward the trailing edge. The growth of the fluctuations for variant 3, which is also representative of variants 1 and 2 in this regard, follows the expected pattern for a transitional boundary layer over a wing, but this is clearly not the case for variant 4. Several questions are posed by these data. First, why are the fluctuations higher for variant 4 than variant 3 at  $x/c = 0.3$  but not at  $x/c = 0.9$ ? Second, why do the higher larger fluctuations at the trailing edge not translate into higher far-field noise levels? The answer to the first question lies in the frequency content of the fluctuations, which is shown in Figs. 18–20 for the smooth wing alongside variants 3 and 4 at  $\eta = 0.01c$  above the surface, which is within the boundary layer. For both the smooth wing and variant 3, the fluctuations on both the sides are dominated by a tonal component of 320 Hz, which corresponds to the T–S instability wave. This frequency is also the dominant frequency in the acoustic field, which again demonstrates that variant 3 exhibits the usual behavior of a growing T–S wave in the boundary layer which then convects over the trailing edge where it scatters as an acoustic wave. For variant 3, the amplitude of the wave grows more substantially on the suction side. This may be due to destabilizing effects of the geometry, or from the lower pressure that occurs over this side when compared to the smooth wing. We also see the growth of fluctuations at multiples of the T–S frequency, which is

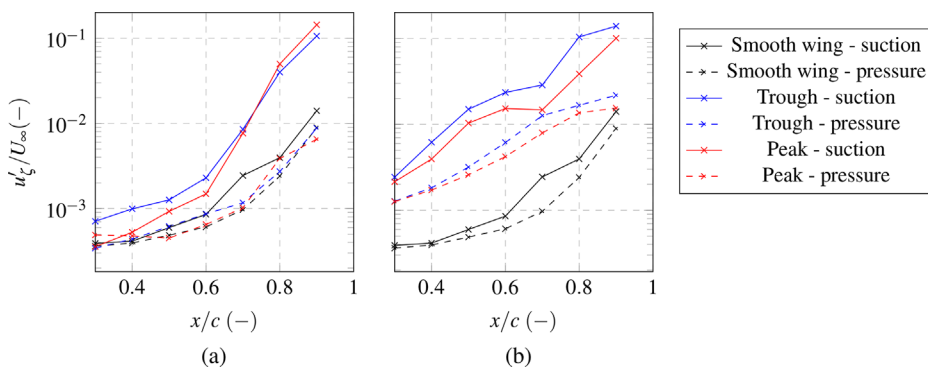


FIG. 17. Average chordwise velocity fluctuations in the boundary layer for (a) variant 3, and (b) variant 4. The fluctuations for the smooth wing are also shown on both graphs for comparison.

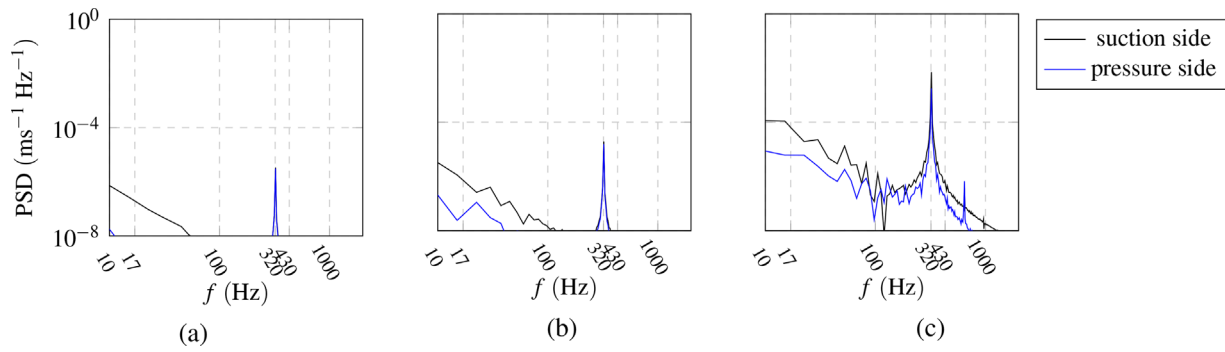


FIG. 18. Power spectral densities of the tangential velocity fluctuations in the boundary layer for the smooth wing at (a)  $x/c = 0.5$ , (b)  $x/c = 0.7$ , and (c)  $x/c = 0.9$ .

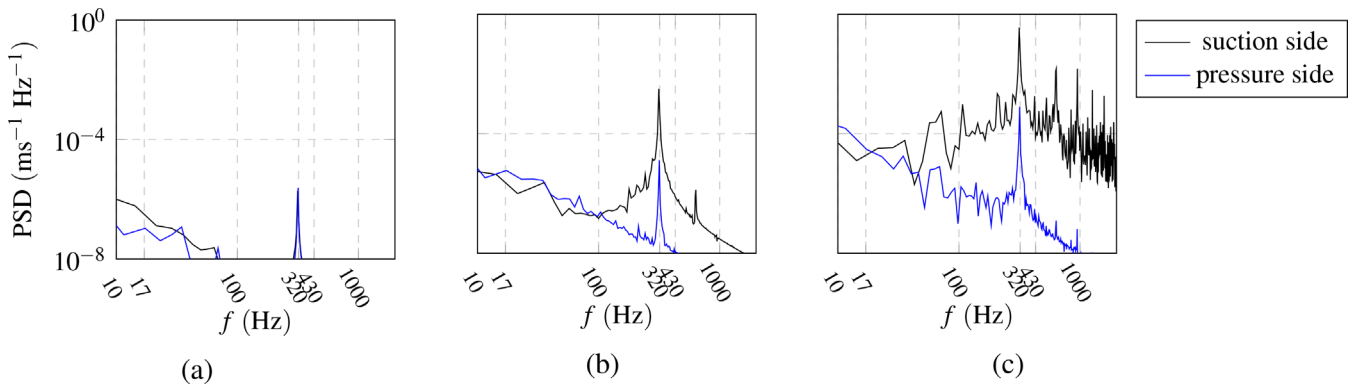


FIG. 19. Power spectral densities of the tangential velocity fluctuations in the boundary layer for variant 3 at (a)  $x/c = 0.5$ , (b)  $x/c = 0.7$ , and (c)  $x/c = 0.9$ .

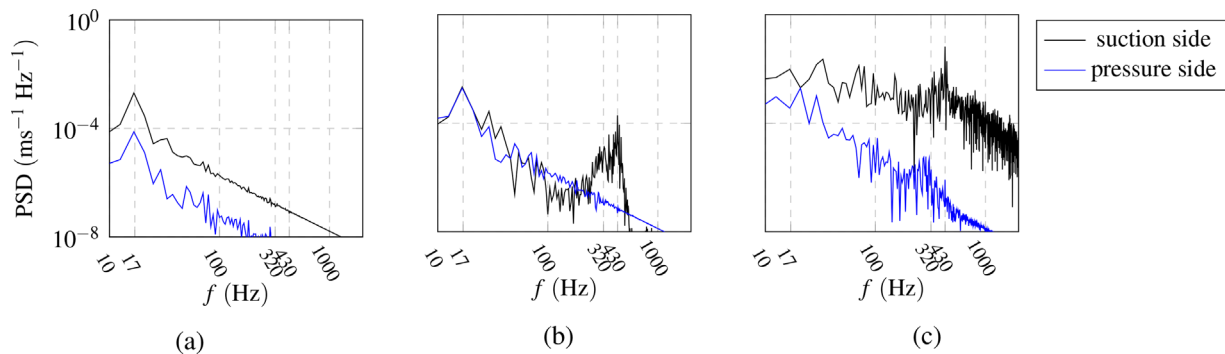


FIG. 20. Power spectral densities of the tangential velocity fluctuations in the boundary layer for variant 4 at (a)  $x/c = 0.5$ , (b)  $x/c = 0.7$ , and (c)  $x/c = 0.9$ .

indicative of the boundary layer entering the final stages of transition, supporting the idea that the geometry does accelerate the transition process. For variant 4, a very different dynamic is observed. There is a low-frequency oscillation in the flow, which grows over the first half of the chord, before stabilizing. This component, with a frequency of

17 Hz, is responsible for the larger fluctuations seen over the first half of the chord in Fig. 17(b). Toward the trailing edge, a growing narrow-band component centered around 430 Hz emerges on the suction side but not the pressure side, and this is the component that is also present in the acoustic spectrum. This is an instability wave, but due to its later

emergence, the amplitude is significantly lower than that of the 320 Hz component for variant 3. There are also phase differences along the span, which further reduce the size of the acoustic source terms produced at the trailing edge. The change in the frequency of this component compared with the other variants is due to its later emergence in the boundary layer. It is largely agreed that the Tollmien–Schlichting waves are produced by a feedback mechanism, whereby the fluctuations produced by the trailing-edge flow propagate upstream where they induce instability waves in the boundary layer of the same frequency. Numerous models and empirical formulas have been proposed for the dominant frequency of the instability,<sup>13,16</sup> and these tend to show an inverse relationship between the feedback length and the dominant frequency. This relationship is also borne out by these results, with the later emergence of the T–S wave implying a shorter feedback length, which in turn results in a higher frequency. Unlike the fluctuations associated with the T–S instabilities, the low-frequency fluctuation observed for variant 4 does not contribute to the acoustic field, as can be seen in the acoustic spectrum in Fig. 13. The reason for this is that the fluctuation has almost no convection velocity and so, unlike the T–S waves, it does not convect downstream and over the trailing edge, and hence, it does not contribute to the acoustic field. This explains why the higher fluctuations in the boundary layer do not lead to higher acoustic intensities. Only those structures that convect over the trailing edge contribute to the acoustic field, with higher convection velocities producing higher acoustic intensities. These dynamics can be clearly seen in Fig. 15(c). For variant 4, the animation of the iso-Q contours shows that the vortical structures that convect over the trailing edge (and hence contribute to the acoustic field) do not emerge until quite close to the trailing edge. The fluctuations that grow over the first half of the chord are not convecting in this manner and so do not contribute. The lack of spanwise correlation in the flow, particularly when compared to the smooth wing and the other variants, is also clear from these animations. The combined effects of the aforementioned dynamics can be seen in the source terms, shown in the top-right pane of Figs. 15(a)–15(c), and also in Fig. 21, which shows the root mean square of the source terms  $S$  on the wing as well as iso-surfaces for  $S = 200$  (green),  $S = 1000$  (orange), and  $S = 10\,000$  Pa/s (red). As well as illustrating the effects of the spanwise correlation and boundary dynamics, this also includes the effect the geometry has on the process whereby the boundary layer fluctuations are scattered at the edge. When comparing variant 3 to the smooth wing, we see that despite having higher fluctuation intensities at the trailing edge, these do not scatter as effectively as acoustic sources due to the effects of the geometry. For variant 4, the combination of the lower fluctuation intensities for the instability wave, the reduction in spanwise correlation, and the geometric effects of the wing on the scattering efficiency lead to a significant reduction in the acoustic sources and hence the radiated noise levels.

#### D. Performance of variant 4 at different angles of attack

Finally, the performance of variant 4 is considered alongside the smooth wing for  $\alpha = 0^\circ$ ,  $2^\circ$ ,  $4^\circ$  to determine whether the large reduction in noise seen at  $\alpha = 1^\circ$  is seen elsewhere. Furthermore, we wish to determine over what range the improvements in lift and drag are seen, and if a penalty is incurred elsewhere. The drag and lift coefficients for the two cases are shown in Fig. 22, and it can be seen here

that the drag coefficient of variant 4 is lower for angles  $\alpha \geq 1^\circ$  but is higher for  $\alpha = 0^\circ$ . The lift and drag benefits of variant 4 appear to be diminishing for higher angles of attack, with only a small reduction in drag, and a slight decrease in lift seen for variant 4 when compared with the smooth wing.

When looking at the radiated noise levels, it is useful to consider them in the context of the expected changes as the angle of attack increases. For a smooth symmetric wing at  $\alpha = 0^\circ$  and operating in a clean uniform flow at a moderate Reynolds number, previous work has shown that the boundary layer fluctuations on the two sides are strongly coupled, leading to a single high-amplitude tone.<sup>45</sup> Secondary tones may also be present, particularly at small non-zero angles of attack or if there is asymmetry in either the flow or geometry. At higher angles of attack, it has been widely reported by many researchers<sup>9,15,55</sup> that the far-field noise reduces significantly. Increasing the angle of attack leads to the suction-side boundary layer transitioning fully to turbulence. The two-dimensional structure of the flow on the suction side is now replaced with a three-dimensional flow with substantially less coherence, which acts as a much weaker acoustic source. On the pressure side, the positive pressure gradient suppresses the growth of the instability waves, thus preventing instability noise from occurring here either. At higher Reynolds numbers, it may be that the boundary layer on both sides is turbulent at low angles and that increasing the angle of attack results in the pressure side becoming transitional, thus allowing instability noise to re-establish.<sup>14</sup> However, this scenario is not relevant here due to the lower Reynolds number.

Figure 23 shows the overall sound pressure level at four different angles of attack for the smooth wing and variant 4. For the smooth wing, the sound levels are as expected, with relatively high levels for the lower angles of attack followed by a sharp drop at  $\alpha = 4^\circ$ . The overall SPL for variant 4 is lower than for the smooth wing at all angles, but there are important changes across the range. At  $\alpha = 4^\circ$ , the overall SPL of the variant 4 is only 1.7 dB lower than the smooth wing, which contrasts sharply with the results seen at other angles of attack. Despite the sharp drop in the noise levels for the smooth wing at  $4^\circ$ , they remain substantially higher than for variant 4 at this angle. The widest difference is seen at  $2^\circ$ , where the overall SPL is 21 dB lower for variant 4 when compared with the smooth wing.

The acoustic spectra at the reference location used earlier are shown in Fig. 24. At  $\alpha = 0^\circ$ , we see much similarity between the smooth wing and variant 4, with both acoustic signatures dominated by a narrowband component, with a frequency of 320 Hz for the smooth wing and 300 Hz for variant 4. This suggests that the boundary layer flow for variant 4 is behaving more like a smooth wing at this angle. At  $\alpha = 2^\circ$ , significant differences in the overall noise levels are seen for the two cases. Both spectra are more broadband than was seen at lower angles, and this is expected as the higher angle of attack promotes the boundary layer on the suction side to transition more readily. Moving to  $4^\circ$ , the noise levels have now dropped significantly for the smooth wing, but they remain above those for variant 4, and there remains a narrowband component centered around 320 Hz, indicating that the boundary layer is still transitional to some degree, and dominated by larger vortices. This helps to explain why the noise levels are still significantly higher than for variant 4. The spectrum for variant 4 still has a small peak at around 430 Hz, which was the frequency of the later emerging and lower amplitude T–S waves seen for



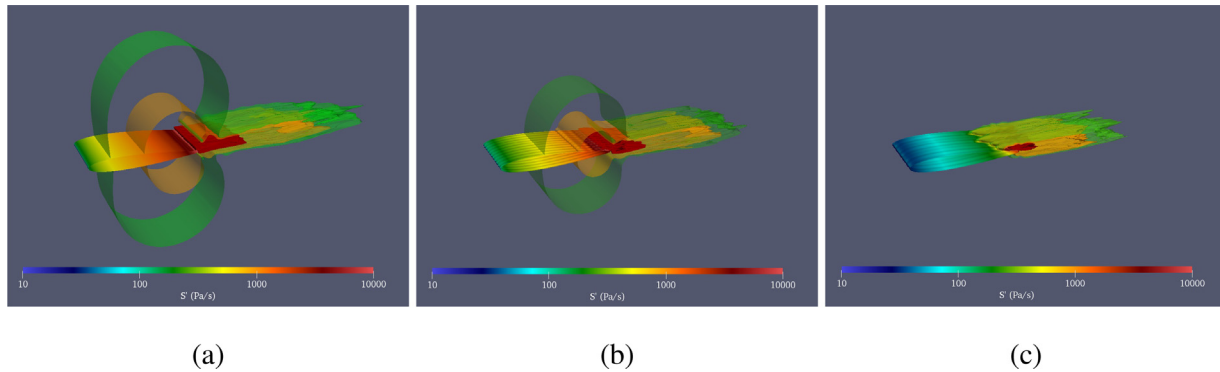


FIG. 21. Root mean square of the acoustic source terms for (a) smooth wing, (b) variant 3, and (c) variant 4. Iso-surfaces are shown for  $S = 200, 1000, 10\,000$  Pa/s.

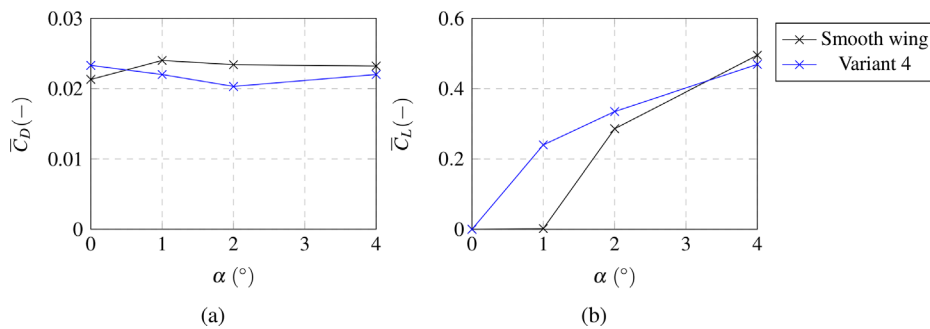


FIG. 22. (a) Drag and (b) lift coefficients for the smooth wing and variant 4 at multiple angles of attack.

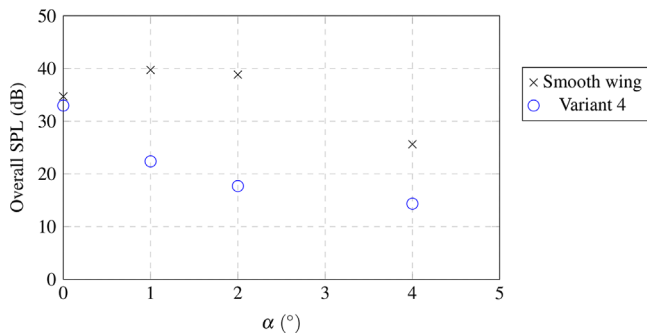


FIG. 23. Overall sound pressure level 1.5 m above the smooth wing and variant 4.

$\alpha = 1^\circ$ . This instability also had a much lower spanwise correlation, which again contributes to the lower radiated noise levels.

These dynamics are echoed by the iso-Q contours, shown for each angle in Fig. 25. For the smooth wing, the changes in the flow field are as one would expect, with the larger angle of attack resulting in the transition process happening further upstream on the suction side. At  $2^\circ$ , the flow at the trailing edge is still broadly two-dimensional, which explains why the noise levels are similar to  $1^\circ$ . At  $4^\circ$ , the transition process is far more advanced at the trailing edge, but it does still retain a level of two-dimensionality, and hence explains the presence of the narrowband component in the acoustic spectrum. The flow over variant 4 is starkly different, particularly at  $2^\circ$  and  $4^\circ$ , where

the flow looks more turbulent, particularly for  $4^\circ$  where the suction-side boundary layer appears turbulent from around mid-chord. At  $\alpha = 0^\circ$ , the flow over the latter half of the chord looks less correlated than for the smooth wing, but at the trailing edge it does exhibit a similar two-dimensionality to the smooth wing.

This is confirmed when considering the spanwise correlation coefficients at  $x/c = 0.9$ , which have been calculated in the same manner as in Sec. III C and are shown in Fig. 26. At  $\alpha = 0^\circ$ , the spanwise correlation is high for both the smooth wing and variant 4. It is noted that this is lower than for the smooth wing at  $\alpha = 1^\circ$ , and this explains why the overall sound pressure level is lower for both wings at  $\alpha = 0^\circ$ . As the spanwise separation increases, the phase difference between the T-S waves increases, which explains the drop in correlation and hence the radiated noise levels for the smooth wing here. The correlation remains high on both sides of the smooth wing at  $\alpha = 2^\circ$ , again explaining the relatively high radiated noise levels here. For variant 4 at  $2^\circ$ , the correlation on the suction side is close to zero, implying incoherent, turbulent flow here. The correlation is higher on the pressure side, owing to the favorable pressure gradient that delays the transition on this side. A similar pattern is seen for variant 4 at  $\alpha = 4^\circ$ , with very low correlation on the suction side. A substantial drop is seen on the suction side of the smooth wing at  $4^\circ$ , which is commensurate with the large drop in sound pressure level, but the correlation remains higher than for variant 4, hence the higher radiated noise levels.

Therefore, as with the cases at  $\alpha = 1^\circ$  discussed in Sec. III C, the changes in the noise levels are due to changes in the boundary layer transition process as well as the spanwise correlation. Most

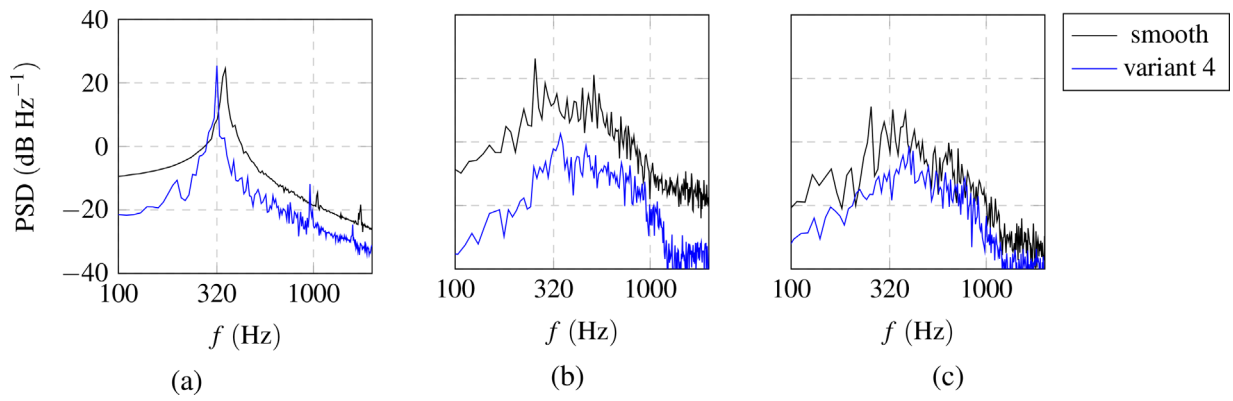


FIG. 24. Sound pressure levels at 1.5 m above the smooth wing and variant 4 for (a)  $\alpha = 0^\circ$ , (b)  $\alpha = 2^\circ$ , and (c)  $\alpha = 4^\circ$ .

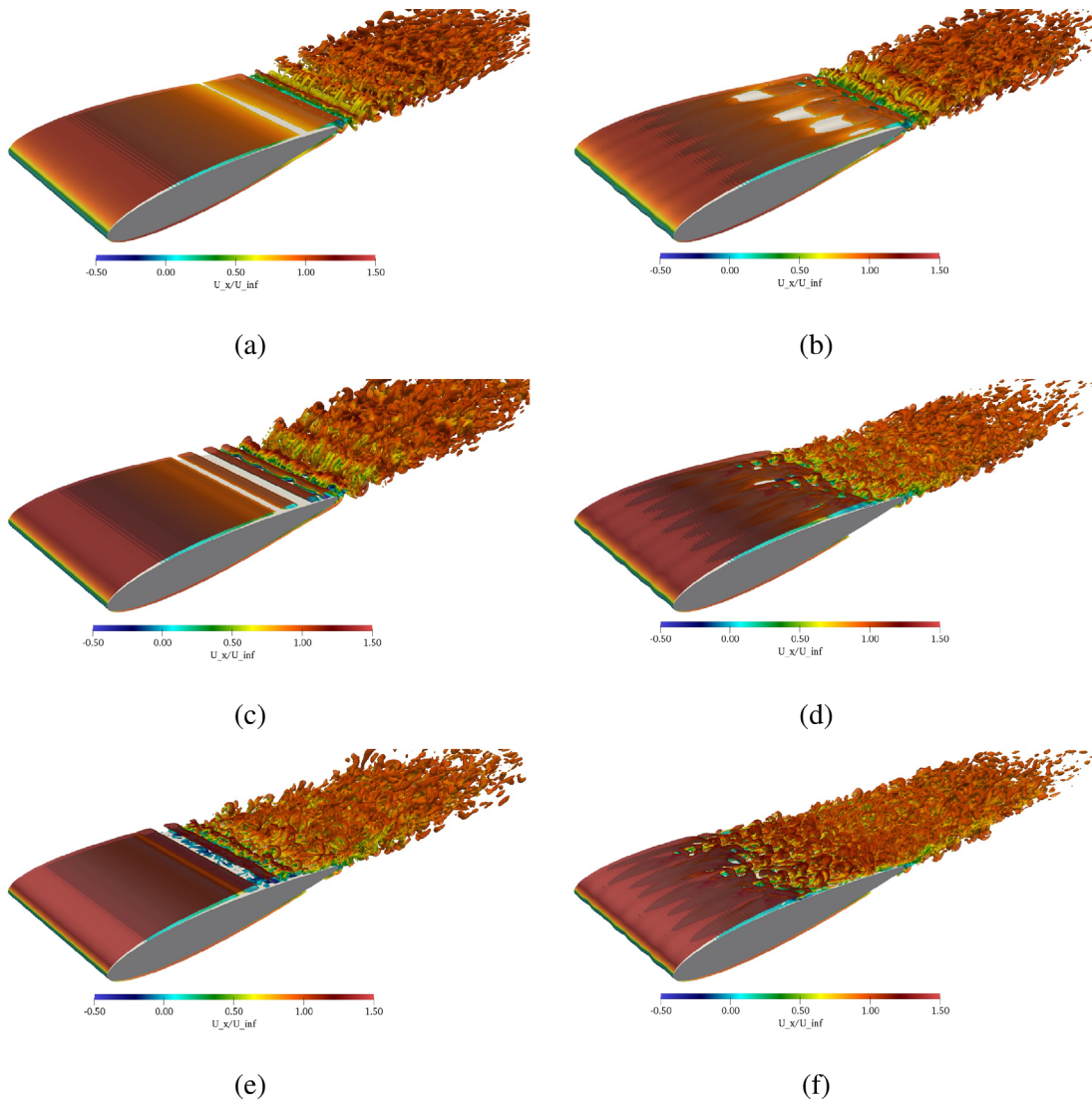
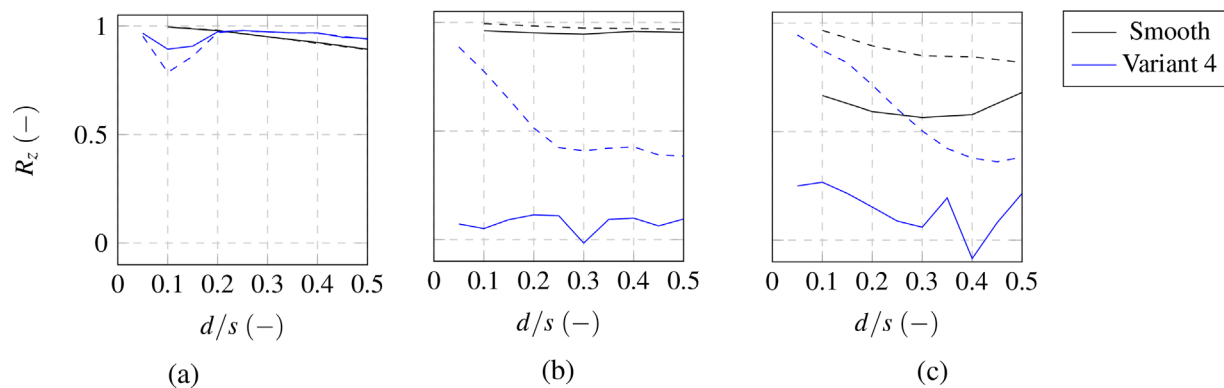


FIG. 25. Iso-Q contours for the smooth wing at (a)  $0^\circ$ , (c)  $2^\circ$ , (e)  $4^\circ$  and variant 4 at (b)  $0^\circ$ , (d)  $2^\circ$ , (f)  $4^\circ$ .



**FIG. 26.** Correlation coefficient of pressure at  $x/c = 0.9$  for (a)  $\alpha = 0^\circ$ , (b)  $2^\circ$ , and (c)  $4^\circ$ . The solid lines denote the suction side (top of wing), and the dashed lines denote the pressure side (bottom of wing).

importantly, the results demonstrate that the wavy wing produces less noise than the smooth wing at all of the angles considered, with substantial reductions seen for  $\alpha \geq 1^\circ$ . Furthermore, this is accompanied by a reduction in drag for  $\alpha \geq 1^\circ$  which demonstrates the potential of this type of geometry for improving aerodynamic and aeroacoustic performance.

#### IV. CONCLUSIONS

In this study, large-eddy simulations have been coupled with the acoustic perturbation equations to investigate the use of spanwise wavy geometries for reducing airfoil self-noise and improving the aerodynamic performance. Four modified NACA0012 airfoils with spanwise waves have been compared to a smooth NACA0012 wing at  $Re = 64\,000$ . The mean and unsteady flow characteristics have been examined together with the acoustic field. Verification and validation has been performed for the smooth wing to provide confidence in the methodology.

It has been found that the drag reduces for variants 2, 3, and 4 when compared with the smooth wing. The mechanism for this has been investigated, and it has been shown that the surface geometry allows for reversed flow in the troughs toward the trailing edge. This reduces the mean shear force over the foil without increasing the overall boundary layer thickness, and so no increase in the form drag is observed. The reduction is greatest for the variants with shorter surface wavelengths. It is not clear at this stage whether these phenomena would be repeated for different Reynolds numbers or geometries, and further investigation into this is warranted.

The results show that all of the wavy geometries produce less noise than the smooth wing, but that a surface wave modified by two waves of different wavelengths is far more effective than a surface wave with only single wavelength. The underlying mechanisms have been examined, showing that variant 4, which has a surface modified by two waves with different wavelengths, has a lower spanwise correlation than the other wings. The boundary layer fluctuations are more broadband, with the instability wave not emerging until much closer to the trailing edge. The total fluctuation intensity in the boundary layer is spread over a much broader range of frequencies and these scatter less effectively as acoustic waves than for the smooth wing, where all of the energy is concentrated at the T-S frequency and the spanwise correlation is very high.

Variant 4 has also been assessed at multiple angles of attack,  $0^\circ \leq \alpha \leq 4^\circ$ , and it has been shown that it produces less noise than the smooth wing over this range. At  $\alpha = 0^\circ$ , there is a higher spanwise correlation, and the T-S instabilities behave much the same as for the smooth wing, leading to only a modest reduction in sound here. However, for  $\alpha \geq 1^\circ$ , both the spanwise correlations reduce substantially, and the dynamics of the boundary layer also change leading to significant reductions in the radiated noise levels.

The results presented here show that wavy geometries can be highly effective at reducing trailing-edge noise, at least at the Reynolds number considered. Further research is now needed to understand the relationship between the surface geometry and noise reduction across a broader range of Reynolds numbers and operating conditions and to try and develop an “optimum” geometry for a given set of conditions. The performance for larger-span airfoils and finite-span wings should also be considered to understand the performance for more industrially relevant configurations. An understanding of the drag reduction mechanism across a broader range of conditions is also needed to determine whether a wavy wing could be a practicable design for reducing both drag and noise across a wider range of conditions than those considered here.

#### ACKNOWLEDGMENTS

The authors wish to acknowledge the use of the UCL Kathleen High Performance Computing Facility and associated support services in the completion of this work.

#### AUTHOR DECLARATIONS

##### Conflict of Interest

The authors have no conflicts to disclose.

##### Author Contributions

**Tom Alexander Smith:** Conceptualization (lead); Formal analysis (lead); Investigation (lead); Methodology (lead); Software (lead); Validation (lead); Writing – original draft (lead); Writing – review & editing (equal). **Christian Klettner:** Conceptualization (supporting); Formal analysis (supporting); Investigation (supporting); Writing – original draft (supporting); Writing – review & editing (equal).

## DATA AVAILABILITY

Raw data were generated at the UCL Kathleen High Performance Computing Facility. Derived data supporting the findings of this study are available from the corresponding author upon reasonable request.

## REFERENCES

- <sup>1</sup>A. Ebrahimi, A. Razaghian, M. Seif, F. Zahedi, and A. Nouri-Borujerdi, "A comprehensive study on noise reduction methods of marine propellers and design procedures," *Appl. Acoust.* **150**, 55–69 (2019).
- <sup>2</sup>W. Dobrzynski and M. Pott-Pollenske, "Slat noise source studies for farfield noise prediction," AIAA Paper No. 2001-2158, 2001.
- <sup>3</sup>D. L. Huff, "Noise reduction technologies for turbofan engines," in *35th International Congress and Exposition on Noise Control Engineering (INTER-NOISE 2006)* (NASA, 2007), p. E-15787.
- <sup>4</sup>K. S. Brentner and F. Farassat, "Modeling aerodynamically generated sound of helicopter rotors," *Prog. Aerosp. Sci.* **39**, 83–120 (2003).
- <sup>5</sup>B. Schäffer, R. Pieren, K. Heutschi, J. M. Wunderli, and S. Becker, "Drone noise emission characteristics and noise effects on humans—A systematic review," *Int. J. Environ. Res. Public Health* **18**, 5940 (2021).
- <sup>6</sup>C. E. Tinney and J. Sirohi, "Multirotor drone noise at static thrust," *AIAA J.* **56**, 2816–2826 (2018).
- <sup>7</sup>T. F. Brooks, D. S. Pope, and M. A. Marcolini, "Airfoil self-noise and prediction," NASA Report No. L-16528 (NASA, 1989).
- <sup>8</sup>W. K. Blake, "Mechanics of flow-induced sound and vibration," *Complex Flow-Structure Interactions* (Academic Press, 2017), Vol. 2.
- <sup>9</sup>T. A. Smith, "Numerical modelling of fluid-induced noise from lifting surfaces at moderate Reynolds numbers," Ph.D. thesis (University College London, 2021).
- <sup>10</sup>S. Oerlemans, P. Sijtsma, and B. M. López, "Location and quantification of noise sources on a wind turbine," *J. Sound Vib.* **299**, 869–883 (2007).
- <sup>11</sup>K. Volkmer, N. Kaufmann, and T. H. Carolus, "Mitigation of the aerodynamic noise of small axial wind turbines-methods and experimental validation," *J. Sound Vib.* **500**, 116027 (2021).
- <sup>12</sup>C. K. W. Tam, "Discrete tones of isolated airfoils," *J. Acoust. Soc. Am.* **55**, 1173–1177 (1974).
- <sup>13</sup>H. Arbey and J. Bataille, "Noise generated by airfoil profiles placed in a uniform laminar flow," *J. Fluid Mech.* **134**, 33–47 (1983).
- <sup>14</sup>E. C. Nash, M. V. Lowson, and A. McAlpine, "Boundary-layer instability noise on aerofoils," *J. Fluid Mech.* **382**, 27–61 (1999).
- <sup>15</sup>T. P. Chong, P. F. Joseph, and M. J. Kingan, "An investigation of airfoil tonal noise at different Reynolds numbers and angles of attack," *Appl. Acoust.* **74**, 38–48 (2013).
- <sup>16</sup>E. Arcondoulis, C. J. Doolan, A. C. Zander, L. A. Brooks, and Y. Liu, "An investigation of airfoil dual acoustic feedback mechanisms at low-to-moderate Reynolds number," *J. Sound Vib.* **460**, 114887 (2019).
- <sup>17</sup>R. D. Sandberg, N. D. Sandham, and P. F. Joseph, "Direct numerical simulations of trailing-edge noise generated by boundary-layer instabilities," *J. Sound Vib.* **304**, 677–690 (2007).
- <sup>18</sup>R. D. Sandberg, L. E. Jones, N. D. Sandham, and P. F. Joseph, "Direct numerical simulations of tonal noise generated by laminar flow past airfoils," *J. Sound Vib.* **320**, 838–858 (2009).
- <sup>19</sup>L. E. Jones and R. D. Sandberg, "Numerical analysis of tonal airfoil self-noise and acoustic feedback-loops," *J. Sound Vib.* **330**, 6137–6152 (2011).
- <sup>20</sup>T. R. Ricciardi, W. R. Wolf, and K. Taira, "Transition, intermittency and phase interference effects in airfoil secondary tones and acoustic feedback loop," *J. Fluid Mech.* **937**, A23 (2022).
- <sup>21</sup>T. R. Ricciardi and W. R. Wolf, "Switch of tonal noise generation mechanisms in airfoil transitional flows," *Phys. Rev. Fluids* **7**, 084701 (2022).
- <sup>22</sup>T. P. Chong and P. F. Joseph, "An experimental study of airfoil instability tonal noise with trailing edge serrations," *J. Sound Vib.* **332**, 6335–6358 (2013).
- <sup>23</sup>L. E. Jones and R. D. Sandberg, "Acoustic and hydrodynamic analysis of the flow around an aerofoil with trailing-edge serrations," *J. Fluid Mech.* **706**, 295–322 (2012).
- <sup>24</sup>D. J. Moreau and C. J. Doolan, "Noise-reduction mechanism of a flat-plate serrated trailing edge," *AIAA J.* **51**, 2513–2522 (2013).
- <sup>25</sup>F. Avallone, W. Van Der Velden, D. Ragni, and D. Casalino, "Noise reduction mechanisms of sawtooth and combed-sawtooth trailing-edge serrations," *J. Fluid Mech.* **848**, 560–591 (2018).
- <sup>26</sup>Y.-S. Hu, Z.-H. Wan, C.-C. Ye, D.-J. Sun, and X.-Y. Lu, "Noise reduction mechanisms for insert-type serrations of the NACA-0012 airfoil," *J. Fluid Mech.* **941**, A57 (2022).
- <sup>27</sup>H. Tian and B. Lyu, "Prediction of broadband noise from rotating blade elements with serrated trailing edges," *Phys. Fluids* **34**, 085109 (2022).
- <sup>28</sup>T. Geyer, E. Sarradj, and C. Fritzsche, "Measurement of the noise generation at the trailing edge of porous airfoils," *Exp. Fluids* **48**, 291–308 (2010).
- <sup>29</sup>I. A. Clark, C. A. Daly, W. Devenport, W. N. Alexander, N. Peake, J. W. Jaworski, and S. Glegg, "Bio-inspired canopies for the reduction of roughness noise," *J. Sound Vib.* **385**, 33–54 (2016).
- <sup>30</sup>V. B. Ananthan, P. Bernicke, R. A. D. Akkermans, T. Hu, and P. Liu, "Effect of porous material on trailing edge sound sources of a lifting airfoil by zonal over-set-LES," *J. Sound Vib.* **480**, 115386 (2020).
- <sup>31</sup>J. Wang, C. Zhang, Z. Wu, J. Wharton, and L. Ren, "Numerical study on reduction of aerodynamic noise around an airfoil with biomimetic structures," *J. Sound Vib.* **394**, 46–58 (2017).
- <sup>32</sup>P. Ball, "Engineering shark skin and other solutions," *Nature* **400**, 507–509 (1999).
- <sup>33</sup>B. Dean and B. Bhushan, "Shark-skin surfaces for fluid-drag reduction in turbulent flow: A review," *Philos. Trans. R. Soc. A* **368**, 4775–4806 (2010).
- <sup>34</sup>P. T. Soderman, "Aerodynamic effects of leading-edge serrations on a two-dimensional airfoil," Technical Report No. NASA-TM-X-2643 (NASA, 1972).
- <sup>35</sup>D. Miklošovic, M. Murray, L. Howle, and F. Fish, "Leading-edge tubercles delay stall on humpback whale (*Megaptera novaeangliae*) flippers," *Phys. Fluids* **16**, L39–L42 (2004).
- <sup>36</sup>K. L. Hansen, R. M. Kelso, and B. B. Dally, "Performance variations of leading-edge tubercles for distinct airfoil profiles," *AIAA J.* **49**, 185–194 (2011).
- <sup>37</sup>A. S. Hersh, P. T. Soderman, and R. E. Hayden, "Investigation of acoustic effects of leading-edge serrations on airfoils," *J. Aircr.* **11**, 197–202 (1974).
- <sup>38</sup>S. Narayanan, P. Chaitanya, S. Haeri, P. Joseph, J.-W. Kim, and C. Polacsek, "Airfoil noise reductions through leading edge serrations," *Phys. Fluids* **27**, 025109 (2015).
- <sup>39</sup>P. Chaitanya, P. Joseph, S. Narayanan, C. Vanderwel, J. Turner, J.-W. Kim, and B. Ganapathisubramani, "Performance and mechanism of sinusoidal leading edge serrations for the reduction of turbulence-aerofoil interaction noise," *J. Fluid Mech.* **818**, 435–464 (2017).
- <sup>40</sup>J. W. Kim, S. Haeri, and P. F. Joseph, "On the reduction of aerofoil-turbulence interaction noise associated with wavy leading edges," *J. Fluid Mech.* **792**, 526–552 (2016).
- <sup>41</sup>P. Chaitanya, P. Joseph, S. Narayanan, and J. Kim, "Aerofoil broadband noise reductions through double-wavelength leading-edge serrations: A new control concept," *J. Fluid Mech.* **855**, 131–151 (2018).
- <sup>42</sup>W. Chen, W. Qiao, F. Tong, L. Wang, and X. Wang, "Numerical investigation of wavy leading edges on rod-airfoil interaction noise," *AIAA J.* **56**, 2553–2567 (2018).
- <sup>43</sup>Y. Lin, K. Lam, L. Zou, and Y. Liu, "Numerical study of flows past airfoils with wavy surfaces," *J. Fluids Struct.* **36**, 136–148 (2013).
- <sup>44</sup>D. J. Moreau, L. A. Brooks, and C. J. Doolan, "The effect of boundary layer type on trailing edge noise from sharp-edged flat plates at low-to-moderate Reynolds number," *J. Sound Vib.* **331**, 3976–3988 (2012).
- <sup>45</sup>T. A. Smith and Y. Ventikos, "A hybrid computational aeroacoustic model with application to turbulent flows over foil and bluff bodies," *J. Sound Vib.* **526**, 116773 (2022).
- <sup>46</sup>R. Ewert and W. Schröder, "On the simulation of trailing edge noise with a hybrid LES/APE method," *J. Sound Vib.* **270**, 509–524 (2004).
- <sup>47</sup>G. Yakhina, M. Roger, S. Moreau, L. Nguyen, and V. Golubev, "Experimental and analytical investigation of the tonal trailing-edge noise radiated by low Reynolds number aerofoils," *Acoust.* **2**, 293–329 (2020).
- <sup>48</sup>W.-W. Kim and S. Menon, "A new dynamic one-equation subgrid-scale model for large eddy simulations," AIAA Paper No. 1995-356, 1995.
- <sup>49</sup>T. A. Smith and Y. Ventikos, "Boundary layer transition over a foil using direct numerical simulation and large eddy simulation," *Phys. Fluids* **31**, 124102 (2019).
- <sup>50</sup>T. A. Smith and Y. Ventikos, "Assessment of computational techniques for the prediction of acoustic sources from lifting surfaces using LES and DNS," in

Eighth International Conference on Computational Methods in Marine Engineering (2019).

- <sup>51</sup>Y. Gao, H. Song, J. Zhang, and Z. Yao, "Comparison of artificial absorbing boundaries for acoustic wave equation modelling," *Explor. Geophys.* **48**, 76–93 (2017).
- <sup>52</sup>M. Drela, "XFOIL: An analysis and design system for low Reynolds number airfoils," in *Low Reynolds Number Aerodynamics* (Springer, 1989), pp. 1–12.
- <sup>53</sup>C. Kato, A. Iida, Y. Takano, H. Fujita, and M. Ikegawa, "Numerical prediction of aerodynamic noise radiated from low Mach number turbulent wake," AIAA Paper No. 1993-145, 1993.
- <sup>54</sup>H. Schlichting and K. Gersten, *Boundary-Layer Theory* (Springer, 2016).
- <sup>55</sup>E. Arcondoulis, C. Doolan, and A. C. Zander, "Airfoil noise measurements at various angles of attack and low Reynolds number," in *Proceedings of ACOUSTICS* (Australian Acoustical Society, 2009), pp. 23–25.